

10. HEAT FLOW EXPERIMENT

The flow of heat from the lunar surface and the associated subsurface temperature fields have evolved from the conditions that existed when the Moon was formed (under the influence of accumulated thermal and structural developments, including those deep in the interior). A knowledge of the present level of surface heat flow may therefore place some important limits on the range of feasible lunar models. To determine this level, instruments capable of making lunar subsurface measurements (from which local heat flow could be derived) were carried to the Moon on the Apollo 15, 16, and 17 missions.

SYMBOLS

The following symbols are used in this discussion of the heat flow experiment (HFE). Because the HFE data output is in degrees Celsius and the experiment was designed accordingly, pertinent discussion must be in degrees Celsius (instead of Kelvin) to avoid misinterpretation by the data user. The International System of Units is used for all other measurements.

$A_{1...6}$	platinum bridge constants determined by calibration
$B_{1...6}$	platinum bridge constants determined by calibration
C	constant
dT/dz	mean vertical temperature gradient
G	system gain
I_E	bridge excitation current
J	heat flow
k	thermal conductivity
\bar{m}	mean value
n	point of constant input ratio

$N_{1...4}$	digital numbers
$N'_{1...4}$	$N - 4096$
R_0	resistance at 0° Celsius
$R_{1...4}$	Wheatstone bridge arm resistances
R_{100}	resistance at 100° Celsius
R_B	total bridge resistance
R_I	idealized output ratio
R_T	resistance at T
T	temperature in degrees Celsius
T_R	reference-bridge temperature
TC	thermocouple
u	digit resolution (2.4412 millivolts)
V^+	positive voltage
V^-	negative voltage
v^+	sensed positive voltage
v^-	sensed negative voltage
v_e	sensed reference-bridge excitation voltage
v_o	sensed reference-bridge output voltage
v_{off}	error offset voltage referred to amplifier input
V_E	bridge excitation voltage
V'_E	sensed bridge excitation voltage

V_L	potential difference across 20-ohm resistance for current I_E
V_O	bridge output voltage
V_T	potential difference across 2-ohm resistance for current I_E
V_X	voltage at connection point X
V_Y	voltage at connection point Y
$X_{1...4}$	calibration constants for reference bridge
z	vertical distance
Z	attenuation ratio V_E'/V_E
α_s	solar absorptance
β	Van Dusen calibration constant
δ	Callendar calibration constant
ΔT	temperature difference in degrees Celsius
ϵ	system error offset
ϵ_O	output-sense-line offset
ϵ_1	excitation-sense-line offset
ϵ_{IR}	infrared emittance
σ	standard deviation

EXPERIMENT THEORY

The heat flow instrument performs measurements to determine the mean vertical temperature gradient dT/dz (where T is temperature in degrees Celsius and z is vertical distance) and the effective thermal conductivity k of the material across

which the measured gradient is developed. Conducted heat flow J diffuses down a temperature gradient in accord with the relationship between these two quantities in one dimension

$$J = -k(dT/dz) \quad (10-1)$$

Table 10-I gives ranges of predicted density of heat flow rate and soil thermal conductivities with the corresponding limits of average temperature gradients.

The average absolute temperature at any point in the subsurface (regolith) results from the balance between the solar heat influx and the total heat outflow acting through the regolith. Solar radiation power incident at the lunar surface varies from 1.45 kW/m^2 at one extreme to 0 at the other extreme. Resultant Moon surface temperatures vary from approximately 400 K at lunar noon to 100 K at lunar night, with an annual modulation of about 8 K caused by the elliptical orbit of the Moon about the Sun. The attenuations and phase shifts of these periodic variations as they propagate into the Moon are determined by the diffusivity of the regolith materials. Nonperiodic variations also occur as a result of changes in the infrared (IR) emittance and solar absorptance of the surface when it is disturbed by the astronauts. Variations were also caused by heat generated during instrument emplacement operations — hole drilling, in particular. To extract meaningful data regarding average gradient from the composite temperatures that may exist at practical lunar measuring depths, the temperature-measuring instrument must have a wider range than the predicted gradients; readings must be recorded frequently for more than a year; and absolute measurement accuracy must equal the relative accuracy requirement for the lowest mean temperature gradient expected.

Two different approaches are used in measuring lunar subsurface thermal conductivity by means of the heat flow instrument. In the first approach, the thermal response of in situ lunar material to known heat sources is tested. In the second, vertical strings of temperature sensors record the characteristics of the periodic propagations into the surface to determine diffusivity; with this diffusivity information and with good estimates of soil mass density and specific heat, thermal conductivity can be calculated.

The first of these approaches takes into account local inhomogeneities, and measurements should sample the volume of material that immediately influences the temperature gradient. Two variations within this approach are required to cover the conductivity range of expected subsurface lunar materials. For soils with low

conductivities (less than 5×10^{-2} W/m-K), a tubular heater wound around one of a pair of temperature sensors vertically separated by 0.5 m is energized with a small amount (2 mW) of power. The rate of rise and the steady-state value of the heated sensor temperature relative to the undisturbed reference level are functions of the thermal coupling from the heater to the lunar material and of the thermal conductivity of the surrounding lunar soil. The temperature rise is inversely proportional to both thermal conductivity and absolute temperature level. Useful range is limited at higher thermal conductivities by reduced sensitivity and by the magnitude of the radiative and conductive thermal resistance of the coupling paths from instrument to soil. For materials such as rock, with conductivities greater than 5×10^{-2} W/m-K, the heater is powered to 0.5 W; the transient and steady-state responses of the lunar medium between the heat source and a remote sensor 0.1 m away are determined by subtracting the characteristic short-time constant response of the intervening sensor support structure from the overall response.

EXPERIMENT DESCRIPTION

The optimum site configuration for the HFE is depicted in figure 10-1. Two hollow fiberglass borestems, 2.5 cm in diameter, are drilled into the lunar surface to a depth of 3 m at a distance of 10 m from each other. Four sets of temperature sensors, spaced along a probe consisting of two flexibly joined rigid sections, occupy the bottom meter of each hole. The sensors, which are primarily radiatively coupled to the borestem and lunar soil, are connected electrically by 8-m woven cables to a package of electronics on the surface. Each cable carries four precisely located thermocouple junctions in the borestems above the probes. The electronics unit is connected to the Apollo lunar surface experiments package (ALSEP) by a 9-m-long flat ribbon cable.

The heat flow instrument returns data that give average-temperature information, differential-temperature information, and low- and high-thermal-conductivity information from four locations on each probe; the thermocouples supply readings for temperature determinations in the upper part of the boreholes. Instrument performance requirements for these measurements are summarized in table 10-II.

In the normal operating mode, the heat flow instrument (1) gathers ambient and high- and low-sensitivity differential temperature data from the gradient sensors situated at the ends of each half-probe section and (2) samples the thermocouple outputs during the 7.25-min measurement sequence. Various sub-sequences can be selected (e.g., measurements on one probe only), but most of them are not normally used. Low-conductivity experiments are

performed on command, with each heater activated in turn to 0.002 W for about 40 hr. The normal measurement sequence is unchanged. The high-conductivity mode of operation requires the selection of measurements on the remote sensors in any half-probe section; the type of data returned alternates between high-sensitivity differential and absolute temperature measurements. Either of the adjacent heaters at the ends of the probe half may be activated by command. Each heater should be on for about 6 hr, but this depends on the conductivity experienced.

EQUIPMENT DESCRIPTION

The platinum resistance sensors used in the HFE probe contribute significantly to the quality of the measurements obtained. Two types of platinum resistance thermometers are used in the heat flow instrument: the so-called gradient sensor and the ring or remote sensor.

Gradient Sensor

The gradient sensor detail is shown in figure 10-2. The sensor incorporates a unique method of supporting the resistance wire to reduce instability normally induced by mechanical or thermal stress. Pure annealed 0.04-mm-diameter platinum wire, coiled in a 0.3-mm-diameter helix that is extended to 0.07 mm pitch, is mounted on a glass-insulated platinum mandrel. The base of each loop is arranged so that only 10 percent of the turn is embedded in the substrate. The mandrel and glass have the same expansion coefficients as the coil, and the assembly is annealed at 673 K for 15 hr before sealing. The platinum coil is isolated from contamination by an atmosphere of pure helium contained within a gold-sealed platinum outer case. Platinum-wire coaxial leads extend through ceramic-insulated tubes for silver brazing to Evanohm and Manganin connecting wires. Each sensor assembly houses two separate elements, effectively bifilar wound, with nominal resistances of 500 Ω at 273.15 K (0° C).

Remote Sensor

The construction of the remote sensor is illustrated in figure 10-3. It consists of two 500- Ω -nominal-resistance platinum wires set in a ceramic glaze around a thin platinum ring. Because the remote sensor is intended for use in the short-term high-conductivity experiments, it has a less stringent stability requirement (0.002 K/6 hr) than the gradient sensor; however, it has demonstrated a long-term stability comparable to that of the gradient sensor.

The sensors are mounted as shown in figure 10-4, which illustrates the configuration common to the ends of all half-probe sections. The gradient assembly is epoxied at the mounting bushing (at the sensor-lead exit end) to the inside of the probe end sheath. The small tube on the opposite end (also shown in figure 10-2) is supported by a snugly fitting fiberglass bushing that permits strain-free differential expansion and good mounting support. Associated with each gradient sensor is a 1000- Ω Karma wire heater, wound concentrically with the gradient sensor on the thin section of the end sheath. The ring sensor platinum band is partially cemented internally to a filler sheath that is attached to the outer sheath of the probe. A tube joins the two end pieces to form a probe half-section.

The structural components providing the span between the sensors were manufactured from low-conductivity, thin-walled, filament-wound epoxy fiberglass. All cabling is carried through the probe body inside the split inner sheath that is shielded with multilayer insulation to reduce radiative coupling between the wiring and probe wall, particularly during conductivity experiments with a heater on. The areas around the sensors are partially enclosed with guards for protection during handling.

A probe assembly is 1.09 m long when unfolded at the closely coiled extension spring that joins the two half-sections. The complete unit is coated with a matte-black thermal control paint. An assembled probe (with its 8-m, 35-conductor connecting cable) weighs less than 0.5 kg.

Gradient and ring sensors are each interconnected within a probe half with AWG 23 Evanohm wire to form bridges, the opposite arms of which are physically situated in the same sensor assembly at a common temperature. A schematic of this resistance bridge arrangement is shown in figure 10-5, where T_1 is the temperature of one sensor assembly and T_2 the temperature of the other. The gradient sensor assemblies, which form one bridge, are separated by 47 cm; the remote sensor assemblies, which form the other bridge, are located 29 cm apart and 9 cm from the heater windings.

Six wires connect each bridge to the electronics unit. Those from a lower half-probe are conveyed in the upper section through the hollow sensor assemblies. Evanohm wire is used because it has a remarkably small temperature coefficient of resistance (0.00002/K), a closely controllable resistivity, and a thermal conductivity that is low for an electrical conductor.

SENSOR CHARACTERISTICS

In Callendar's empirical parabolic equation

$$T = 100 \left(\frac{R_T - R_0}{R_{100} - R_0} \right) + \delta \left(\frac{T}{100} - 1 \right) \frac{T}{100} \quad (10-2)$$

the constant δ defines the characteristics of an individual platinum resistance thermometer over the temperature range 0° to 630° C, where T is temperature in degrees Celsius, R_T is resistance at temperature T , R_0 is resistance at 0° C, and R_{100} is resistance at 100° C. The Callendar constant is determined by calibration at the following three fixed points: the triple point of water (0.0100° C), the steam point (100° C), and the boiling point of sulfur (444.600° C). For use between 0° and -183° C, a correction term devised by Van Dusen is added to the Callendar equation to give

$$T = 100 \left(\frac{R_T - R_0}{R_{100} - R_0} \right) + \delta \left(\frac{T}{100} - 1 \right) \frac{T}{100} + \beta \left(\frac{T}{100} - 1 \right) \left(\frac{T}{100} \right)^3 \quad (10-3)$$

where the constant β for an individual thermometer is found by calibrating at the boiling point of oxygen (-182.97° C). The resistance of one platinum element at temperature T relative to its resistance at 0° C is therefore

$$\frac{R_T}{R_0} = 1 + \frac{1}{100} \left(\frac{R_{100}}{R_0} - 1 \right) \left[T - \delta \left(\frac{T}{100} - 1 \right) \frac{T}{100} - \beta \left(\frac{T}{100} - 1 \right) \left(\frac{T}{100} \right)^3 \right] \quad (10-4)$$

Referring to figure 10-5, the bridge voltage ratio is defined

$$\frac{V_O}{V_E} = \frac{R_1 R_4 - R_2 R_3}{(R_1 + R_3)(R_2 + R_4)} \quad (10-5)$$

where R_1 , R_2 , R_3 , and R_4 are Wheatstone bridge arm resistances; V_E is the excitation voltage across the bridge; and V_O is the output voltage. By combining equations (10-4) and (10-5) and eliminating small terms, the following simplified expression is obtained:

$$\begin{aligned} \frac{V_O}{V_E} R_B = & A_1 + A_2 T + A_3 T^2 + A_4 \Delta T + A_5 \Delta T (\Delta T + 2T) \\ & + A_6 [\Delta T (4T^3 - 300T^2) + \Delta T^2 (6T^2 - 300T) \\ & + \Delta T^3 (4T - 100) + \Delta T^4] \end{aligned} \quad (10-6)$$

where R_B is total bridge resistance; T is the temperature of one sensor assembly expressed in degrees Celsius; ΔT is the temperature differential between sensor assemblies in degrees Celsius; and A_1 , A_2 , A_3 , A_4 , A_5 , and A_6 are constants. Similarly, bridge resistance R_B can be related to temperature T and temperature differential ΔT by the simplified expression

$$\begin{aligned} R_B = & B_1 + B_2 T + B_3 T^2 + B_4 (T - 100) T^3 + B_5 \Delta T \\ & + B_6 \Delta T (\Delta T + 2T) \end{aligned} \quad (10-7)$$

where B_1 , B_2 , B_3 , B_4 , B_5 , and B_6 are constants. Equations (10-6) and (10-7) are transcendental in T and ΔT . To find absolute and differential temperatures, an iterative simultaneous solution of both calibration equations is required.

ELECTRONIC MEASUREMENT SYSTEM

System Operation

Equations (10-6) and (10-7) show that the electrical measurements required to solve for T and ΔT are total bridge resistance R_B (measured as a single element), excitation voltage V_E , and differential output voltage V_O . The system by which these measurements are made is represented in the simplified block diagram in figure 10-5, which includes the essential features of the bridge measurement method. The diagram includes only one of the eight probe bridges and omits thermocouple circuits, power supplies, and most of the logic and control circuits.

Each of the bridges is selected through reed relays for excitation by direct current. The bridges produce a differential output-to-input voltage ratio V_O/V_E of approximately $+5.8 \times 10^{-3}$ for a dynamic range of ± 2 K. With 8 V applied to the bridge excitation cables, the data-chain maximum input requirement is set at ± 34 mV. The gradient bridge low-sensitivity range of ± 20 K requires 0.8 V excitation for a similar output maximum. Measurements for total bridge resistance are made at the 8-V supply level. Excitation voltage V_E is reduced to the maximum level of the output voltage by an attenuator in the excitation sense circuit.¹ The output impedance is arranged to be the same as the bridge differential output impedance. At the low-sensitivity excitation level of 0.8 V, the attenuator output V_E is one-tenth of the maximum bridge unbalance voltage V_O at ± 20 K temperature extremes. To effectively normalize these readings and at the same time avoid attenuator switching or gain changes, excitation current I_E is sensed. This current is combined with the total bridge resistance value determined from readings at 8-V excitation made within a short time of the current measurement) to calculate the low-level-excitation supply voltage. Low-sensitivity current is found from the potential difference V_L developed across a precision 18- Ω plus 2- Ω resistance in the supply line; high-sensitivity current is found from the potential difference V_T across the 2- Ω resistor only. The latter value is used with the attenuated bridge-excitation-voltage measurement

¹The series elements of the attenuator include cable resistance that does fluctuate slightly with the large surface-temperature variations, but the proportion of cable resistance in the temperature-matched attenuator is small, and very high attenuation-ratio stability is achieved.

to determine total bridge resistance R_B . Differential output voltages are read directly.

These various measurements are presented sequentially through a low-level field effect transistor (FET) multiplexer to the input of the common signal amplifier, which has a gain of 288 and a full-scale output of ± 10 V. The amplified signal is converted to a 13-bit digital number and clocked into a shift register along with a 7-bit mode-identification and binary-measurement code. The resulting 20-bit number is serially shifted into the ALSEP central station for insertion as two 10-bit words into the ALSEP data stream for transmission to Earth. On Earth, the binary numbers are converted back to the sensor temperatures from which they originated by applying the calibration factors for each bridge or thermocouple and each measuring channel. The sources of error to which the reconverted temperature values may be subject are as follows:

1. Platinum bridge error sources
 - a. Initial calibration accuracy
 - b. Element stability with age
 - c. Dissimilar metal electromotive forces at sense-wire connections
2. Measurement system error sources
 - a. Initial calibration of electronics
 - b. System noise
 - c. Spurious electromotive forces in multiplexer
 - d. Excitation voltage
 - (1) Stability
 - (2) Sense-attenuation stability
 - (3) Bridge heating
 - e. Amplifier
 - (1) Common-mode rejection
 - (2) Gain and offset stability

(3) Linearity

(4) Settling time

f. Analog-to-digital converter

(1) Linearity

(2) Reference voltage stability

(3) Quantizing magnitude

3. Data-processing error sources

a. Truncation errors

b. Iterative solution accuracy of bridge equations

Ratio Measurement Technique

Errors due to long-term system gain and offset instability are circumvented by a scheme that paradoxically amounts to a calibration of each measuring channel by the unknown signal being measured. A ratio technique is used that eliminates system gain and offset as factors in the reconstitution of the original bridge ratio. The success of the technique depends only on gain and offset stability during the brief measurement period. All measurements are made twice (at two different levels). To utilize the full system range and obtain maximum resolution, it is convenient for each bridge input and output measurement to be made at reversed polarity and with equal bipolar excitation levels. The bridge is pulsed twice in 2.4 sec for 2.6 msec at a maximum duty cycle (0.2×10^{-3}) that limits self-heating to an acceptable $0.1 \mu\text{W}$; two measurements are made during each excitation pulse. The sequence outlined in figure 10-6 for a high-sensitivity differential measurement is typical of all measurements. Power is applied to the bridge from the excitation-pulse supply at bipolar 4-V levels, which gives a positive 8-V total excitation. After 1 msec to allow the system to settle, the attenuator output V_E^+ corresponding to excitation level V_E^+ is converted to a digital number N_1 . Output voltage V_O^+ is then selected for measurement; and, after a 2.3-msec positive pulse duration, V_O^+ conversion to N_2 is executed. The entire process is repeated 2.4 sec from the start of the sequence with the pulse-excitation supply output reversed to -8 V; during application of this negative

pulse, $V_E'^-$ and V_O^- are converted to digital numbers N_3 and N_4 , respectively.

If G represents amplifier and analog-to-digital-converter gain

$$\begin{aligned} \frac{N_2 - N_4}{N_1 - N_3} &= \frac{G(V_O^+ + \epsilon_O + \epsilon) - G(V_O^- + \epsilon_O + \epsilon)}{G(V_E'^+ + \epsilon_1 + \epsilon) - G(V_O^- + \epsilon_1 + \epsilon)} \\ &= \frac{V_O^+ - V_O^-}{V_E'^+ - V_E'^-} \end{aligned} \quad (10-8)$$

$$= \left(\frac{V_O^+}{V_E'^+} \right) \left(\frac{1 - \frac{V_O^-}{V_O^+}}{1 - \frac{V_E'^-}{V_E'^+}} \right)$$

where ϵ is the amplifier and analog-to-digital-converter offset, ϵ_O is the output-sense-line offset, and ϵ_1 is the excitation-sense-line offset. Because the temperature of a bridge in the lunar regolith will not change during the 2.4-sec measurement period

$$\frac{V_O^+}{V_E'^+} = \frac{V_O^-}{V_E'^-} = C \quad (10-9)$$

where C is a constant regardless of the excitation magnitudes of $V_E'^+$ and $V_E'^-$. Rearranging equation (10-9) to read

$$\frac{V_O^-}{V_O^+} = \frac{V_E'^-}{V_E'^+} \quad (10-10)$$

and combining equations (10-8) and (10-9) results in

$$\frac{N_2 - N_4}{N_1 - N_3} = \frac{V_O^+}{V_E'^+} \quad (10-11)$$

where $V_O^+/V_E'^+$ is the ratio between measured bridge signals, independent of gain and offset. The required bridge ratio V_O/V_E is obtained by applying the excitation-sense measurement attenuation factor Z , the accuracy and stability of which clearly affect the result. Since $Z = V_E'/V_E$, then

$$\frac{V_O}{V_E} = \frac{ZV_O}{V_E'} \quad (10-12)$$

Other Design Features

The use of excitation-polarity reversal, with one data converter for all measurements, eliminates some major sources of error and obviates the need for separate periodic calibrations on the Moon and for additional circuitry with which to perform them. Nevertheless, numerous sources of error remain. It is therefore pertinent to summarize here the more significant features of the principal components of the data chain, which account for demonstrated measurement accuracies of better than 0.02 percent full-scale probable error over a temperature range of 273.15 to 333.15 K (0° to 60° C).

The pulsed-power supply produces $4000 \text{ V} \pm 1 \text{ mV}$ bipolar pulses that are stable to within 0.002 percent during bridge excitation and output measurements. The supply operates from positive and negative reference levels, which are derived from constant-current-driven, low-temperature-coefficient zener diodes that are switched by the control logic for positive and negative bridge excitation outputs from two series-connected operational amplifiers. Each amplifier has a push/pull output stage to supply the 20-mA bridge current.

The multiplexer for the heat flow instrument is a double-tiered N-channel FET commutator, with 32 differential input pairs. It is divided into four sections, one for each probe set of gradient sensors and one each for the remote sensors and the thermocouples. Each FET section is powered only when necessary to restrict the effects of a single-channel failure. The FET

temperature-dependent offset voltages and mismatched differential impedances, which act with circuit impedances and amplifier bias currents to introduce variable offset voltages for each channel and different offsets between channels, are canceled by the ratio measurement technique previously described.

The most basic design trade-offs in analog-to-digital converter design are speed and accuracy; neither is of great consequence in this application, where extreme linearity, stability, and sensitivity are the only critical requirements. Digital conversion of the amplified sensor signals is achieved by 13-bit successive approximation to the sum of a generated $+10.000\text{ V} \pm 1\text{ mV}$ offset supply and the $\pm 10\text{-V}$ full-scale output from the data amplifier. The offset binary number produced is linear to within 0.0075 percent full scale, with a resolution of 2.4414 mV per bit. Conversion speed is 20 μsec per bit. The device is a conventional successive-approximation analog-to-digital converter, with the two most significant bits of the ladder network trimmed to remove errors due to voltage drops across the switches.

The signals are amplified by a differential-input single-ended-output two-stage amplifier, with differential and common-mode impedances exceeding 50 and 20 $\text{M}\Omega$, respectively, at frequencies below 5 kHz. The common-mode rejection ratio is greater than 120 dB over the same frequency range. The characteristics most important to the ratio technique are linearity, which is within 0.005 percent full scale, and short-term stability, which is better than 0.001 percent for 5 sec at a maximum rate of temperature change of 0.01 K/sec (0.01° C/sec). The common-mode rejection ratio becomes important when bridge current is sensed at 8-V excitation levels.

Constant-current sources are supplied to each base of the differential input pair to compensate for the bias current required by the matched semiconductors, but the more usual constant-current-source common-emitter supply is replaced with a variable current source that maintains the constant output of combined collector currents. The differential output from the collectors connects to an operational amplifier, the output of which feeds back to the emitters of the input stage to force the total of the collector currents to divide equally between the two halves of the differential pair. Stable operating points are thus established independently of common-mode inputs over a wide temperature range. The first-stage gain is 100. After filtering, the signal is applied to the input of the second-stage amplifier that normally operates with a gain of 2.88. The total amplifier gain of 288 is used for all bridge measurements.

Thermocouple measurements require an input range of $\pm 10\text{ mV}$ rather than $\pm 34\text{ mV}$. During thermocouple sequences, therefore,

the second-stage gain is changed from 2.88 to 10 by switching an FET to introduce a potential divider in the feedback path of the second stage.

THERMOCOUPLE MEASUREMENTS

Eight Constantan and two Chromel wires from the thermocouple junctions in the probe cables connect to Kovar leads at an isothermal block inside the electronics package. The Kovar leads convey the thermocouple voltages to the multiplexer. The isothermal block also contains a platinum/Evanohm bridge thermometer with two constant-value resistance arms. A schematic that represents one probe-cable set of thermocouple junctions and the reference-temperature bridge is presented in figure 10-7.

Thermocouple measurements of absolute temperature have an inherent accuracy an order of magnitude lower than platinum resistance measurements in part because of thermocouple instability, but primarily because of difficulties in measuring low-level voltage sources. Because the ratio technique is not applicable to thermocouple measurements, a calibration method is used to establish system gain and offset during the measurement sequence to find the isothermal block temperature with the bridge thermometer.

Measurements on the reference-temperature bridge follow the same pattern as those on the probe bridges, except that the amplitude of excitation is attenuated to give a ± 10 mV full-scale output, which is the range of the thermocouple voltages. An amplifier nominal gain of 1000 is selected for reference-bridge and thermocouple measurements. To find system gain and error offset values, it is assumed that the attenuated positive and negative bridge excitation voltages V_E are of known, equal, and opposite magnitudes because they are derived from the precisely controlled pulsed-power supply and are connected to the bridge by short leads within the electronics package.

The sensed excitation signals v_e^+ and v_e^- are converted by the analog-to-digital converter to binary numbers N_1 and N_3 in accord with the relationships

$$\left. \begin{aligned} N_1 &= \frac{G(v_e^+ + v_{\text{off}})}{u} \\ N_3 &= \frac{G(v_e^- + v_{\text{off}})}{u} \end{aligned} \right\} \quad (10-13)$$

where v_{off} is error offset voltage referred to the amplifier input and G is system gain. The full-scale, 13-bit binary output count is 0 to 8191, which corresponds to an offset amplified signal range of 0 to 20 V and gives a digit resolution u of 2.4414 mV. Gain is found from

$$G = \frac{u(N_1 - N_3)}{v_e^+ - v_e^-} \quad (10-14)$$

when the offset voltages cancel. To find the error offset voltage v_{off} , the offset binary outputs N_1 and N_3 are converted to positive and negative numbers by subtracting offset count 4096. If $N'_1 = (N_1 - 4096)$ and $N'_3 = (N_3 - 4096)$, then

$$v_{\text{off}} = u \frac{N'_1 + N'_3}{2} \quad (10-15)$$

The use of known balanced inputs in the reference bridge measuring sequence thus establishes system gain and offset. The measured outputs are converted through electronics calibration data, and the bridge voltage ratio is then used to solve iteratively a third-order calibration equation for reference-bridge temperature and hence for isothermal-block and reference-thermocouple temperature. Measurements of thermocouple voltages made shortly thereafter (in the sequence N_1 , N_2 , N_3 , and N_4 as shown on the fig. 10-7 schematic) are processed by using calculated gain and offset values to arrive at true thermocouple voltage outputs.

The output from the Chromel/Constantan reference junction in the isothermal block is measured relative to only one of the junctions in the cable — the junction inside the hollow of the gradient sensor at the top of the probe. The remaining three junctions in each probe cable are also measured relative to this top junction. The double-referencing arrangement is designed to center the mean of the thermocouple output extremes close to 0 V for maximum measurement resolution. The predicted temperature range for the thermocouple junction at the top of the probe is 200 to 260 K; the full-scale thermocouple range is 90 to 350 K, and the isothermal-block temperature is controlled to between 278 and 328 K.

The voltage/temperature characteristics of the thermocouples are described by calibration correction factors applied to standard tables of the National Bureau of Standards (NBS).

PACKAGE CONSTRUCTION AND THERMAL CONTROL

The heat flow instrument operates from a 29-V dc supply and requires data-interlace and mode-control signals from the ALSEP central station. The unit is otherwise self-contained with respect to logic and power management for all the sensor measurements and for probe-heater control.

In the deployed configuration, a ribbon cable consisting of 40 flat copper conductors in a plastic film extends from the instrument package across 9 m of the lunar surface to the ALSEP central station. This cable is connected to an astromate connector that the astronauts mated with the ALSEP central station outlet for power to and communication with the heat flow instrument.

The two probe cables each consist of 35 unshielded conductors, interwoven for a uniform stress distribution so that the weight of the astronaut can be supported without degradation in cable performance. These cables are very flexible and exhibit little residual torque when extended; they are covered with a woven Teflon sleeve to provide a low coefficient of friction during deployment. Heatleaks from the cables on the lunar surface to the probes and the electronics package are small because the conductors are made from wire that has low thermal conductivity.

Electronics Package

The electronics package is made up of five multilayer printed-circuit boards that are joined in a stack by interlocking spacers bonded to each board. The stack is 6 by 19 by 14 cm (2.5 by 7.6 by 5.6 in.); the boards consist of as many as

12 layers, each 0.1 mm (0.004 in.) thick. The layers of circuit tracks are interconnected through plated holes in the composite board, and as many as 210 component subpackages are mounted on one board. The components are in physical contact with a heavy printed-circuit conductor that forms a heat path to the interlocking spacers. Column screws pass through the spacers to a metal plate that serves as a thermal control plate and as a support for the board stack. A dc/dc converter for the instrument power supplies is packaged on a board that is bonded to the thermal control plate. Heating elements are also mounted in good thermal contact with the plate. A short length of Manganin cable provides thermal insulation from the copper conductors in the ribbon cable. Bonded to the thermal control plate at the other side of the unit is a 70-pin isothermal connector to which the two probe cables are soldered. When the unit is assembled, the board stack is enclosed by a metal cover with a compressible, electrically conducting gasket to provide a barrier to electromagnetic interference.

Thermal Control Design

A thermal insulation bag, shaped as a container for the metal cover surrounding the board stack, is hooked by Velcro pads to a low-thermal-conductivity mounting ring fitted around the inside edge of the thermal plate. The bag is constructed of 12 layers of closely spaced, high-reflectivity shields that have very low transverse conductivity; bridal-silk netting separates the layers and covers the inside and outside of the bag. The IR emissivity of the 0.00064 cm (0.25 mil) aluminized Mylar used for the shields is approximately 0.02.

The electronics assembly is supported and protected by a thin fiberglass outer case that is connected to the mounting ring by low-conductivity joints. When the unit is standing on the feet of this outer case, the well-insulated electronics compartment is situated beneath the exposed thermal control plate. Internally generated heat is conducted to the plate and radiated from a spectrally selective surface coating having a high IR emittance ($\epsilon_{IR} = 0.9$) and a low absorptance ($\alpha_s = 0.2$) at frequencies where solar power is most intense.

This simple thermal control arrangement could not modify the extreme heat of solar radiation as well as the cold of deep space in the tenuous atmosphere of the Moon to meet the required electronics-temperature operating range (278 to 328 K) without using excessive power during lunar night or permitting the upper limit to be exceeded during lunar day. The thermal plate is therefore protected from direct solar radiation by a sunshield fitted over the assembly. The sunshield is an insulated box with one open side, which is placed to face away from the equator with its edge aligned in the east/west direction. The numbered marks

on the sunshield are used as a shadowgraph; the shadow is cast by the universal handling tool that fits into the center socket. A specular reflector slopes from the top edge of the sunshield at an angle of 57° from vertical and almost touches the thermal plate. The reflector increases the view of the thermal radiator plate to the near-absolute-zero temperature of space and minimizes the lunar-surface-radiation reflections that reach the thermal plate from the exposed inside surfaces of the enclosure. The side curtains adjoining the sloping reflector are also specular surfaces. The reflecting mirrors are produced by a vacuum process in which a thin layer of aluminum is deposited on polished fiberglass. The back of the reflector and the thermal control plate inside the sunshield are heavily blanketed with aluminized Mylar, layered in the same way as in the thermal bag. The concealed interior surfaces of the sunshield are also coated with metal by a vacuum process to reduce radiant interchange of IR energy inside. The exterior surfaces of the entire package are covered with thermal control coating.

A mast of multilayer insulation is attached to the edge of the thermal plate to prevent direct sunlight from reaching it in the event of a moderate misalignment from an east/west line or an instrument-leveling error. To aid in leveling in the stark lighting of the Moon, the bubble level situated at one corner on a recessed platform is illuminated by reflection of sunlight from the vertical wall of the step.

The thermal control design for the heat flow instrument is dictated largely by the power dissipation of the unit at lunar noon. The average dissipation is minimized by gating off as many circuits as possible when they are not required for measurements. During power gating, the average operational power dissipation is 3.9 W. The power-sharing mode is set to switch in when thermal plate temperatures exceed 300 K. During lunar night, when the electronics temperature falls below 290 K, additional power is dissipated by the heaters on the thermal control plate. The thermal control system is designed for instrument deployment between lunar latitudes of $\pm 45^\circ$.

CALIBRATION AND TESTING

To ensure that the heat flow instrument would meet its performance requirements, the calibration and test program was extensive and thorough. A substantial part of the large array of calibration and test apparatus used was developed specifically for this purpose. The sensors, probes, and electronics were subjected to worst-case mission environments and were calibrated as subunits before assembly as flight instruments. The subassembly calibrations were verified by tests on the complete unit, which then underwent a further series of tests closely simulating all the

conditions anticipated for travel to and operation on the Moon. After exposure to such critical environments as system vibration, the stability of the instrument was carefully checked.

Sensors

The platinum resistance thermometers were calibrated as a bridge by a comparison method. Each sensor, together with a standard thermometer, was immersed in an isothermal bath of trichloroethylene. The baths had separate temperature controls so that temperatures could be independently set for each thermometer of the differential bridge. The standard thermometers were interchanged for several measurements to determine offset. The unit of measure (Kelvin) was established from standard thermometers calibrated by the NBS. Secondary absolute-value resistance standards of 1000 Ω , referenced to an NBS standard, were maintained for the electrical measurements.

To check for random errors, each gradient bridge was calibrated at 42 points, which were least-squares fitted to equations (10-6) and (10-7) to yield the 12 constants in these equations. The standard deviation of the least-squares fit to the data points in equation (10-6), did not exceed 0.48×10^{-3} K for any of the sensor assemblies tested, and more than 60 such assemblies have been produced. The gradient bridges were calibrated at differential temperatures of +20, +10, +2, 0, -1, -2, -10, and -20 K; they were calibrated at absolute temperatures of 200, 212.5, 225, 237.5, and 250 K. The equivalent differential-temperature drift of some randomly selected gradient sensors tested periodically at 200 and 270 K over a 3-yr period was approximately 0.3×10^{-3} K. The average absolute-temperature drift for individual sensor elements over the same 3-yr period was 0.5×10^{-3} K. The ring sensors were calibrated at a minimum of 14 points to calculate 12 calibration constants.

Thermal-plate reference-temperature bridges in the electronics package were calibrated at 253, 273, 298, 323, and 363 K (-20°, 0°, +25°, +50°, and +90° C) to yield the constants X_1 , X_2 , X_3 , and X_4 in the relationship

$$\frac{V_O}{V_E} = X_1 + X_2(T_R) + X_3(T_R)^2 + X_4(T_R)^3 \quad (10-16)$$

where T_R is the reference bridge temperature and V_O/V_E is the bridge voltage ratio. During reference-bridge calibration at 273 K (0° C), all eight cable thermocouple junctions were immersed in an isothermal bath for calibration at 90, 200, 250, and 350 K.

Electronics

Testing of the electronics data chain involved adjustment by resistance-value selection for zero offset, common-mode rejection, and gain. A calibration factor was found for each measuring channel by calibrating the channel as it would be used; that is, by performing ratio measurements. A set of resistance networks, calibrated to an accuracy of 0.002 percent, was substituted for bridge and line resistances to simulate high-sensitivity and low-sensitivity ratios and bridge resistance. The various types of measurements were made through separate channels. Calibration was performed at 9 different differential-ratio amplitudes and 5 levels of bridge resistance; at least 10 measurements were made for each of the input ratios. The mean \bar{m} and standard deviation σ of the output ratios for a constant input were calculated, and a linear calibration factor was found from the mean values corresponding to ratios near the limits of channel range ($n = 1$ and $n = 9$ in fig. 10-8). The ideal transfer function of the channel was the calibration factor. The error at any point n was defined as the difference between the ideal output $R_1(n)$ and the mean output $\bar{m}(n)$, summed with the standard deviation $\sigma(n)$. To verify system linearity, these measurements were made at temperature intervals throughout the operating range of the heat flow instrument. A maximum error of 0.0375 percent full scale was specified, but the typical maximum for instruments tested to date has been 0.02 percent. Calibration factors were modified for the actual bridge-lead resistances. Thermocouple channel accuracy was also checked by multiple measurements at nine points throughout the ± 10 mV input range.

Probes

Assembled probes were characterized over ambient- and differential-temperature operating ranges in a temperature-gradient apparatus (gradient chamber) that had an overall height of 3.4 m (11 ft) and a diameter of 0.6 m (2 ft). The probes were inserted in a gradient tube (2.5 cm internal diameter) in which a positive or negative temperature field could be developed. A liquid-nitrogen bath surrounded the gradient-tube assembly to provide a constant-temperature heat sink for heat introduced in developing average and linear differential temperatures. A double-vacuum shell minimized heatleaks and permitted the probe to be inserted without unduly disturbing the thermal equilibrium. Thermocouples

and thermopiles in the gradient tube, along with associated readout instrumentation, provided accuracies of temperature measurement that approximated those of the heat flow instrument. Probe-measured differential temperature was compared with apparatus-measured differential temperature in the form of a "shorting" ratio, which was approximately a linear function of the absolute temperature along the gradient; the probes were radiatively coupled to the gradient tube. This shorting ratio varied from bridge to bridge because of small differences in probe construction. The probes were tested at mean ambient temperatures of 205, 225, and 245 K, with linear gradients of 0, 2, and 18 K across each probe half-section. At least five tests were performed with each flight-instrument probe, including two tests in which the probe was integrated with electronics. Tests in the gradient chamber at 0 K checked the zero offset of the gradient bridges and determined the offset values for the ring bridges, the cables of which were shortened during probe assembly. Each of the probe heaters was turned on at the 0.002-W level by the electronics to characterize the low-conductivity performance of the probe in an infinitely conducting environment, which the gradient-tube apparatus represented since it was an almost perfect heat sink.

Thermal conductivity testing was also performed in an apparatus that simulated the properties of the lunar regolith. In essence, this thermal conductivity test apparatus was a 3.2- by 0.9-m (10.5- by 3-ft) Dewar flask, with inner-vessel-wall cooling to the temperature range 200 to 250 K. A probe boretube extended into a bed of glass microbeads in the inner container. The outer cavity and the boretube were evacuated, and the thermal conductivity of the glass-bead bed was varied over the anticipated lunar range by controlling the gas-filling pressure. Two thermal conductivity test units were constructed to permit the simultaneous testing of the two probes of a heat flow instrument.

Heat Flow Instrument

For functional testing of the probes and the heat flow instrument as a whole, thermal simulators were used to provide a stable temperature environment for the probes in the lunar-temperature operating range. Each simulator was an insulated container 2.5 m (8 ft) deep, filled with solid carbon dioxide and ethanol, in which a heavy metal double boretube was vertically situated. The ethanol fluid stabilized at the temperature of the subliming dry ice that it surrounded. Because the temperature of sublimation is a function of pressure, the fluid temperature increased with depth to impose a gradient along the boretubes. Thermocouples and thermopiles within the metal block measured the temperature profile along the tubes. The laboratory thermal simulator had a compartment for the electronics package so that the whole instrument could be operated in a vacuum. When inserted

into the boretubes, the two probes of the instrument were in a similar, uncontrolled but slowly changing temperature field; and comparisons could be made of processed measurements on the probe bridges at given heights in the bath.

A comparable simulator was built into an adjunct of an 8.3- by 6.2-m (27- by 20-ft) thermal vacuum chamber. During ALSEP system testing, the heat flow electronics package was deployed inside the main chamber, with the probes situated in the stabilized thermal simulator boretubes. The entire ALSEP system, including the heat flow instrument, was exposed to the temperature conditions of lunar dawn, lunar noon, and lunar night in a vacuum of 6.7×10^{-6} N/m² (5×10^{-8} torr). Cold space was simulated in the chamber by pumping liquid nitrogen under pressure through black, optically tight panels. Solar heat was simulated by the use of carbon arc lamps, and dust degradation on instrument surfaces was simulated by subjecting them to additional IR radiation.

Table 10-III presents a comparison of thermal-simulator temperature measurements made in a changing temperature environment by the heat flow instrument probes and electronics package during simulated lunar-night testing of the Apollo 16 ALSEP system. The means of the differences between the temperatures measured by adjacent bridges, which have been corrected for bridge shorting ratio, and the standard deviations from the means are tabulated. The very small differences noted may have been caused by differences in the transient responses of the two probes; by different probe responses to nonlinear gradients; or by slightly different temperature fields, the result either of inherent differences between the apparatus boretubes or of different times of measurement. Aside from these factors, the probe-measurement differences reflect the consistency of total instrument calibration, stability, and signal processing.

The low-sensitivity measurements on the upper gradient bridges illustrate an effect of data averaging that is generally seen in heat flow instrument test results. Although resolution in the ± 20 K range is 10 times less than in the high-sensitivity range — a fact reflected by the standard deviations — the averages are about the same in the two ranges. The number of measurements that did not follow this pattern decreased as the number of data cycles increased. Thus, system resolution was effectively increased by multiple-measurement averaging in both the low- and high-sensitivity ranges. Use of this technique can result in an effective resolution that is better than analog-to-digital-conversion quantization would allow for a single measurement.

During the simulated lunar-night test in which these results were obtained, the probe cables were lying in an uncontrolled temperature zone. There is little value, therefore, in comparing thermocouple readings 2, 3, and 4. However, the mean of the

measurement differences for the thermocouples situated at the top of the probes (0.073 K) relative to the single-measurement resolution of 0.17 K again demonstrates the data-averaging effect. The readings also provide a good comparative check of the thermocouples.

OPERATIONAL HISTORY

Apollo 15

Probe configuration.- The heat flow probes were not buried to the planned depth of the experiment because of difficulties in drilling holes into the regolith. A map of the probe placement relative to other ALSEP experiments is shown in figure 10-9, and the subsurface configuration of the probes is shown in figure 10-10.

Initiation of the experiment.- Times important to the initiation of the Apollo 15 experiment (in 1971) are as follows:

<u>Event</u>	<u>Day</u>	<u>Hr, G.m.t.</u>
Probe 1 insertion	212	18.78
Probe 2 insertion	213	17.28
Instrument turn-on	212	19.47

Ring-bridge surveys.- In mode 1, full sequence, the temperatures at the ring-bridge sensors are not measured. To obtain measurements at these thermometers, the experiment is periodically commanded to mode 3 with heaters off, and all bridge sensors are sampled by sending the appropriate sequence of commands. This procedure is called a ring-bridge survey. Initially, the surveys were taken frequently, every 6 hr; they have been continued to the present time with a longer interval between samples. The routine schedule beyond the real-time postmission support is three ring-bridge surveys weekly.

Conductivity measurements.- During real-time support, conductivity experiments at low power, 0.002 W, were run on the following schedule:

Heater location	Depth, cm	Heater on -		Heater off -	
		Day	Time, hr:min, G.m.t.	Day	Time, hr:min, G.m.t.
1971					
H11	35	242	17:00	243	17:00
H12	83	247	05:04	248	16:55
H13	91	238	04:58	239	16:57
H14	138	245	05:01	246	16:55
H23	49	236	05:00	237	17:01
H24	96	250	05:00	251	17:00
1972					
^a H11	35	073	15:01	075	15:00
^a H12	83	045	14:42	047	02:26

^aThese positions were rerun because they were strongly affected by diurnal variations, and more optimal times were selected to decrease transient variations during the observation.

Eclipses.- During total eclipses, the experiments are commanded into the thermocouples-only mode.

Photographs used in analysis.- The following lunar surface photographs were used in the analysis: AS15-87-11849, 87-11860, 92-12407 to 92-12409, 92-12416, and 92-12421. These photographs are available at the National Space Science Data Center (NSSDC).

Apollo 16

The cable connecting the heat flow electronics package with the ALSEP central station was inadvertently broken during ALSEP deployment activities, rendering the experiment hardware inoperative.

Apollo 17

Probe configuration.- The probes were both buried to the desired depth. A map of the probe placement relative to other ALSEP experiments is shown in figure 10-11, and the configuration of the probes in the subsurface is shown in figure 10-12.

Initiation of the experiment.- Times important to the initiation of the Apollo 17 experiment (in 1972) are as follows:

<u>Event</u>	<u>Day</u>	<u>Hr, G.m.t.</u>
Probe 1 insertion	347	02.730
Probe 2 insertion	347	03.133
Instrument turn-on	347	03.033

Ring-bridge surveys.- Ring-bridge surveys are run on approximately the same schedule as that of the Apollo 15 experiment.

Conductivity measurements.- All eight experiments at low power were run during the real-time support period (1973) by the following schedule:

Heater location	Depth, cm	Heater on -		Heater off -	
		Day	Time, hr:min, G.m.t.	Day	Time, hr:min, G.m.t.
H11	130	003	05:58	004	18:00
H12	177	014	00:03	015	11:48
H13	185	021	00:03	022	12:31
H14	233	008	06:21	009	16:02
H21	131	005	05:18	007	06:07
H22	178	016	12:06	018	00:05
H23	186	023	00:31	024	12:30
H24	234	010	05:59	011	17:59

On day 25, 1973, at 18:00 G.m.t., H14 was turned on at high power, 0.5 W. After 3 hr of observation, the ring bridge (DTR12) went off-scale high and the heater was shut off at 20:30 G.m.t.

Photographs used in analysis.- The following lunar surface photographs were used in the analysis: AS17-134-20493 to 20497, 147-22590 to 22600, 147-22602, and 147-22603. These photographs are available at the NSSDC.

INSTRUMENT MALFUNCTIONS

Instrument malfunctions as of December 10, 1973, were as follows:

1. Apollo 15: The data channel for the reference thermometer stopped operating August 7, 1971. This channel is redundant, and no data have been lost.
2. Apollo 16: The cable was broken at the ALSEP central station plug. One probe was deployed. The instrument is inoperative.
3. Apollo 17: The only significant problem is the very high noise level of the thermocouples during the lunar day just before noon.

SUMMARY OF RESULTS

During the Apollo missions, two heat flow measurement sites were successfully established on the lunar surface. Both measurement sites are in similar regional settings in the northeast quadrant of the Moon. The Taurus-Littrow and Rima Hadley sites are located in embayments in the mountainous rims of the Imbrium and Serenitatis mascon basins that have been flooded by mare-type basalts.

Surface brightness temperatures were calculated from the temperature of the thermocouples suspended several centimeters above the lunar surface. The mean surface temperature at Rima Hadley throughout a lunation cycle is 207 K. The mean temperature increases with depth very rapidly in the upper few centimeters and is approximately 252 K at a depth of 90 cm. The main reason for this increase of 45 K is the predominant role of radiative heat transfer in the loosely packed upper layer. During the lunar night, the surface temperature at Rima Hadley falls to 93 K. From the cooldown history after sunset, it was deduced that the upper 2 cm of the regolith is characterized by a conductivity of 1.5×10^{-5} W/cm-K. Below this depth, the conductivity increases rapidly and probably in a continuous manner until it reaches values of approximately 1.5×10^{-4} W/cm-K at depths where the probes are emplaced.

At Taurus-Littrow, the mean surface temperature is 216 K and, as in the case of Rima Hadley, increases a few tens of degrees in the upper 2 cm so that, at a depth of 67 cm, a mean temperature of 254 K is measured. The minimum temperature just before lunar dawn is 103 K, 10 K higher than that at Rima Hadley. This higher temperature is primarily attributable to the existence of a relatively high conductivity layer at a depth 2 cm below the surface. From the point of view of thermal properties, the regolith at Taurus-Littrow can be described as two layers: (1) an upper 2-cm, loosely packed layer of very low conductivity (1.5×10^{-5} W/cm-K) in which heat transfer by radiation predominates and (2) a lower layer with much higher conductivity ($>1.2 \times 10^{-4}$ W/cm-K) and higher density (1.8 to 2.0 g/cm³).

Subsurface temperature and conductivity measurements at depths below 90 cm, where the large diurnal variations are negligibly small, indicate a steady-state heat flow through the surface at Rima Hadley of 3.1×10^{-6} W/cm² and at Taurus-Littrow of 2.8×10^{-6} W/cm² with an estimated error of ± 20 percent. Temperature and conductivity data are given in tables 10-IV to 10-VIII. These fluxes are deduced from average temperature gradients in the regolith between 1.3 and 1.7 K/m and an average conductivity in the range of 1.7×10^{-4} to 2.0×10^{-4} W/cm-K. Conductivity generally increases with depth in the regolith, although some layering (high conductivity materials overlying lower conductivity materials) is found at both sites. A conductivity value of almost 3×10^{-4} W/cm-K was measured at the bottom of probe 1 at the Apollo 17 site. In some cases, thermal gradients decrease with depth in response to the increase in conductivity. At Taurus-Littrow probe site 2, a large decrease in gradient with depth is possibly attributable to a large subsurface boulder close to the probe.

The heat flows at both sites are affected to some extent by local topography. Preliminary estimates indicate that a correction of -15 to -25 percent may be applicable to the Taurus-Littrow values because of the adjacent massifs. However, a more refined analysis is required.

The heat flow measured at the two sites is approximately one-half of the average heat flow of the Earth (6.3×10^{-6} W/cm²). If these two values are representative of heat flow from the Moon as a whole, then a heat flow of one-half that of the Earth requires a heat production per unit mass for the lunar interior of more than twice that of the Earth. This statement assumes both planetary bodies are near steady state so that total surface heat loss is nearly equal to the present interior heat production.

Because the long-lived radioisotopes of potassium-40, uranium-235, uranium-238, and thorium-232 are the principal source of heat in the Earth and Moon, the heat flow results imply a two-fold to threefold enrichment of uranium in the Moon relative to that in the Earth. Lunar samples show that the abundance of potassium relative to uranium is one-third to one-fourth that of the Earth so that, in the Moon, uranium is the main contributor to internal heating. At present, these isotopes must be concentrated in the outer 100 to 200 km of the Moon to avoid extensive melting at shallow depth.

Reinterpretation of Earth-based measurements of microwave brightness temperatures using the new data on regolith thermal and electrical properties will be important in determining the representativeness of the in situ lunar heat flow measurements. Additional and more refined microwave observations of the Moon, especially narrower beamed measurements over discrete portions of the lunar disk, would be valuable in determining possible variations of heat flow over the lunar surface.

LONG-TERM DATA ANALYSIS

Figure 10-13 shows the 3.5-yr absolute temperature histories at representative Apollo 15 and 17 probe sensors. Three distinct temporal components are apparent in the data: (1) A diurnal component (period = 29.53 days) is evident at the sensors closest to the lunar surface. Below approximately 80 cm, the almost 300 K peak-to-peak surface variation is attenuated to a level below the noise of the absolute temperature measurements. (2) Temperature variations of 1-yr period are detectable at all sensors within 120 cm of the surface. Although the annual variation in mean surface temperature due to the eccentricity of the Earth-Moon orbit about the Sun is only approximately 3 K peak-to-peak, the amplitude attenuation is only $1/\sqrt{12.37}$ that of the diurnal variation. A significant annual component is evident in the more accurate temperature difference data at depths up to 200 cm at the Apollo 17 site. (3) At all sensors, there is an aperiodic temperature rise that is characterized by a decreasing magnitude and increasing time delay before onset at greater depths. These transients were initiated during experiment emplacement when astronaut activity disrupted the thermal and radiative properties of the surface material surrounding each borestem. The subsequent effects of local changes in mean surface temperature are detectable at all subsurface sensors. It is estimated that reequilibration of the deepest sensors to the new steady state regime will require 5 to 7 yr.

Refinement of Subsurface Temperature Profiles

The identification and removal of diurnal, annual, and transient variations and the corrections for shallow sensor radial fluxes allow reliable temperature profiles to be calculated at the Apollo 15 probe 2 site and the upper section of probe 1. Only the probe 1 lower-section results have been previously reported for Apollo 15. Figure 10-14 shows the steady-state temperature profiles at the Apollo 15 and 17 sites. Corrections at the Apollo 15 probe 1 lower section and at both Apollo 17 stations due to transient and annual effects were quite small (less than 5 percent) and the results are largely unchanged from those reported previously (refs. 10-1 and 10-2).

The temperatures shown at 65 cm at the Apollo 17 stations are thermocouple measurements that are substantially less accurate than the probe sensor results. Except for probe 2 of Apollo 17 (65-cm temperature), all profiles are remarkably linear, suggesting a vertical uniformity of bulk regolith thermal properties at probe depths. The gradients indicated were calculated from a linear least squares fit to the probe sensor results. The anomalously low gradient at the Apollo 17 probe 2 appears to increase significantly at shallower depths and may indicate a local disturbance to the heat flow, because no comparable change in thermal conductivity is indicated by the analysis.

Revised Regolith Conductivity and Lunar Heat Flow

The determination of regolith conductivity from the revised diffusivity results requires specification of the regolith volumetric heat capacity. The specific heat of a number of lunar particulate samples have been measured (ref. 10-3). Results indicate substantial variation with temperature but almost no variation from sample to sample. A value of 0.67 W-sec/g-K, measured at 250 K, is used for all probe depth conductivity calculations.

The bulk densities of drill core samples have been reported by Carrier (ref. 10-4). The results from the Apollo 15 drill core indicate densities that range from 1.75 to 1.84 g/cm³ from depths of 40 to 160 cm. Because of disruption of the soil during drilling, these data probably represent minimum estimates of the in situ values. Maximum density measurements on Apollo 15 soils of 1.89 ± 0.03 g/cm³ were obtained by Carrier (ref. 10-4). Thus, a reasonable range of densities to use for converting the Apollo 15 diffusivity estimates to thermal conductivities is 1.75 to 1.90 g/cm³. Similar results for Apollo 17 soils lead to an estimated range of 1.83 to 2.09 g/cm³.

Revised results are shown in figure 10-15. On the left, the thermal conductivities deduced from the long-term analysis are compared with the point measurements made by the heater experiment designed into the probe and reported earlier. Notice that these new determinations are significantly lower than the earlier measurements. The fact that the difference between the old and new measurements increases with depth suggests that the difference may be due to increasing compaction of the regolith around the drill stem as the stem penetrated deeper and deeper.

Revised (solid line) and preliminary (dashed lines) heat flow results are shown at the right in figure 10-15. The lowered heat flow values are accounted for almost entirely by the revised conductivity determinations. At the Apollo 15 site, a heat flow value of $2.1 \mu\text{W}/\text{cm}^2$ is the mean of the two probe measurements; and, at Apollo 17, the probe 1 value of $1.6 \mu\text{W}/\text{cm}^2$ is considered the more reliable measurement. Errors of the measurements, deriving primarily from the resolution constraints of the annual wave diffusivity deductions, are estimated at ± 15 percent.

FUNCTIONAL FLOW OF DATA REDUCTION

A flow diagram for the reduction of one lunation of data is given in figure 10-16. Descriptions of the computer programs are given in the following paragraphs.

PROG6 (Diagnostic Dump of JSC Tape)

The PROG6 program reads the NASA Lyndon B. Johnson Space Center (JSC) tape and prints the header records and the data records on an online printer. The printout includes record number, time, station identification, bit error rate, data rate, frame number, and ALSEP word 33 (that is, word 33 (ordinal) of the 64 10-bit binary words (640 bits) that constitute one frame of the ALSEP bit stream which spans an interval of 54/90 sec). The ALSEP word 33 is given as a decimal equivalent of 10 binary bits. The program recognizes end of tape (EOT) marks and will call exit upon encountering one. The following errors generate error messages:

1. Permanent read error in a record (code = 3)
2. Short record (code = 7)
3. Long record (code = 5)

PROG8 (Intermediate Reduction) and Intermediate Data File

The PROG8 program reads the JSC tape and prints the header record on an online printer. Further (optional) printout includes record numbers (in and out), time, station identification, bit error rate, data rate, frame number, and ALSEP word 21 (that is, word 21 (ordinal) of the 64 10-bit binary words (640 bits) that constitute one frame of the ALSEP bit stream which spans an interval of 54/90 sec). The ALSEP word 21 is given as a decimal equivalent of 10 binary bits. The program recognizes EOT marks and will call exit and rewind the JSC (input) tape upon encountering an EOT. The following errors generate error messages and stop execution:

1. Permanent read error in a record (code = 3)
2. Short record (code = 7)
3. Long record (code = 5)

The output of this program, which is stored in the "Intermediate data file (disk file 19)," is the same data that appear in the (optional) printout.

The usual sampling sequence for the HFE (mode 1, sub-sequence 1; or full sequence) includes all the data points except those for the ring bridges. A full sequence covers an interval of 7.2 min in the ALSEP bit stream. (Two consecutive ALSEP 21 words are required for one "N-value"; four consecutive N-values constitute one data point; one full sequence consists of 16 consecutive data points; and the HFE has allocated to it frames 0 through 15 of every 90 frames (54 sec).) The routine reduction procedure only stores every eighth usable full sequence of data in file 19. If the full density option is being exercised, or if the sampling sequence is other than usable mode 1 sub-sequence 1, all the available data are stored in file 19. There are also provisions for printing and/or storing and/or dumping bad or unusable data if such is desired.

PROGP (Complete Reduction) and Reduced Data File

The PROGP program reads the "Intermediate data file (disk file 19)" and reduces the ALSEP 21 words to temperatures and temperature differences. The reduced data for one lunation are stored on tape and in disk file 17. Associated with each complete sequence of data points is the time corresponding to when the sequence began and a code word containing mode, sub-sequence, and heater state. (The disk data contain the mode and sub-sequence information implicitly and do not contain the heater state information.) The routine reduction procedure reduces all the data

that are in disk file 19 unless it is considered necessary to reduce the data density further (e.g., to satisfy storage requirements (2400 records in disk file 17 or one tape per lunation)) in which case any desired density can be obtained for a particular sampling mode and sub-sequence. The online printout for PROGPs consists of mode changes, reduced data sequences (optional), and/or errors that occur therein (optional), and/or bad or unusable data (optional). There are also provisions for storing and/or dumping bad or unusable data if desired.

DATAL (Postreduction Processing), Lunation Printout, and Lunation Plots

The DATAL (datalook) program has three independent functions all of which operate on or from disk file 17 (reduced data for one lunation):

1. Reading the reduced data tape for a lunation and storing the data in file 17. This function is rarely used and is intended primarily to cover mistakes in the routine postreduction processing.

2. Printing all the reduced data for one lunation on the online printer from file 17. Two copies of this printout are routinely made; one for the permanent reduced data file at the Lamont-Doherty Geological Observatory (L-DGO) and one for NASA. The printout format consists of two identical title pages that specify lunation, days of the year spanned by the lunation, and the year in which the lunation occurs, followed by the lunation data in the following three sets.

- a. Probe 1 data for modes 1 and 2 with summary statistics.
- b. Probe 2 data for modes 1 and 2 with summary statistics.
- c. Mode 3 data for both probes with summary statistics

3. Plotting all the reduced data for one lunation from disk file 19. The original plot is stored in the L-DGO permanent reduced data file. Three 50-percent (black-and-white) reproductions are made for distribution to the principal investigators and other interested people. The data for each sensor (or pair of sensors in the case of gradients) are plotted separately except for the thermocouples, four of which are superposed on one grid with the reference bridge temperature for that probe. The plots are arranged to facilitate comparison of sensor data for different sensors. Superposed on the time axis of each plot is a Sun angle

grid for relating sensor data with the Sun's position as seen from the experiment.

HFA21, HFA22, and the Master Disk Files

The HFA21 and HFA22 programs transfer to master disks OA21 (probe 1) and OA22 (probe 2), respectively, the lunation of data residing in the reduced data file (disk file 17). The data for each pair of sensors are stored in a separate file except in the case of thermocouples, which are all stored in one file with the corresponding reference bridge temperature for that probe. The data in each file are in chronological order. There is also a file of file pointers for bookkeeping purposes. When the data are transferred, two modifications are performed.

1. The correct time for each data point is computed by adding a constant to the time the data point sequence began, where the constant depends on when the data point occurs in the sequence. This correct time is stored with the data on the master disk.

2. The temperatures and temperature differences are converted to integer values, which permits storage of up to 3 yr of data for one probe on one disk.

THE L-DGO MASTER DISK ORGANIZATION

For each experiment, all data are stored on two L-DGO master disks, one for each probe. Each disk can hold approximately 3 yr of data, and each disk consists of six files that are described as follows.

<u>File</u>	<u>Description of data</u> ²	<u>Length of record</u>	<u>Maximum number of records in file</u>
1	T and ΔT of upper section gradient bridge	4 disk words ³	30 000
2	T and ΔT of lower section gradient bridge	4 disk words	30 000
3	Thermocouple temperatures	8 disk words	30 000
4	T and ΔT of upper section ring bridge ⁴	4 disk words	1 200
5	T and ΔT of lower section ring bridge ⁴	4 disk words	1 200
7	Present record count for each file and time of last record on disk	7 disk words	1

THE L-DGO NSSDC TAPES

The L-DGO tapes prepared for NSSDC are described here. Machine format specifications: 7 track, 800 bpi, standard IBM interrecord gap, odd parity, data convert "on," translate "off." There is no end of file.

²The first two disk words in each record on files 1 to 7 give the time in milliseconds since 00:00 January 1, 1971, for Apollo 15; since 00:00 January 1, 1972, for Apollo 17 as a floating point variable.

³To save space, the data are converted from real to integer format by multiplying by an appropriate power of 10 and truncating the meaningless fractional part (which is smaller by an order of magnitude than the precision of the apparatus).

⁴Each data point in this file is the average of about 10 contiguous values measured during a ring-bridge survey.

Data organization: There is one 183-m (600-ft) tape for each probe, and there are five groups of data on each tape. (Size of physical record for each group equals 100 logical records.)

<u>Group</u>	<u>Type of data</u>	<u>Size of logical record</u>
1	Time, T, and ΔT of upper section gradient bridge	3 real words
2	Time, T, and ΔT of lower section gradient bridge	3 real words
3	Time, T, and ΔT of upper section ring bridge	3 real words
4	Time, T, and ΔT of lower section ring bridge	3 real words
5	Time, blank, reference bridge and thermocouple temperatures	7 real words

Each tape contains data for a period of 1 yr.

DATA ARCHIVED AT NSSDC

As a year of reduced L-DGO data become available, the data are transferred to a magnetic tape (one for each probe) from the master disks with no modifications or editing. These tapes with documentation are sent to NSSDC.

REFERENCES

- 10-1. Langseth, M. G., Jr.; Clark, S. P., Jr.; Chute, J. L., Jr.; Keihm, S. J.; and Wechsler, A. E.: Heat-Flow Experiment. Sec. 11 of Apollo 15 Preliminary Science Report. NASA SP-289, 1972.
- 10-2. Langseth, Marcus G., Jr.; Keihm, Stephen J.; and Chute, John L., Jr.: Heat Flow Experiment. Sec. 9 of Apollo 17 Preliminary Science Report, NASA SP-330, 1973.
- 10-3. Hemingway, B. S.; Robie, R. A.; and Wilson, W. H.: Specific Heats of Lunar Soils, Basalt, and Breccias from the Apollo 14, 15 and 16 Landing Sites, Between 90 and 350 K. Proceedings of the Fourth Lunar Science Conference, vol. 3, Pergamon Press (New York), 1973, pp. 2481-2487.
- 10-4. Carrier, W. David, III: Apollo Drill Core Depth Relationships. The Moon, vol. 10, no. 2, 1974, pp. 183-194.

BIBLIOGRAPHY

- Ade, P. A.; Bastin, J. A.; Marston, A. C.; Pandya, S. J.; and Puplett, E.: Far Infrared Properties of Lunar Rock. Proceedings of the Second Lunar Science Conference, vol. 3, A. A. Levinson, ed., MIT Press (Cambridge, Mass.), 1971, pp. 2203-2211.
- Baldwin, J. E.: Thermal Radiation from the Moon and the Heat Flow Through the Lunar Surface. Monthly Notices, Roy. Astron. Soc., vol. 122, 1961, pp. 513-522.
- Bassett, H. L.; and Shackelford, R. G.: Dielectric Properties of Apollo 14 Lunar Samples at Microwave and Millimeter Wavelengths. Proceedings of the Third Lunar Science Conference, vol. 3, David R. Criswell, ed., MIT Press (Cambridge, Mass.), 1972, pp. 3157-3160.
- Buhl, D.; Welch, W. J.; and Rea, D. G.: Anomalous Cooling of a Cratered Lunar Surface. J. Geophys. Res., vol. 73, no. 24, Dec. 15, 1968, pp. 7593-7608.
- Carslaw, H. S.; and Jaeger, J. C.: Conduction of Heat in Solids. Clarendon Press (Oxford), 1959, pp. 64-69.
- Conel, J. E.; and Morton, J. B.: Interpretation of Lunar Heat Flow Data. The Moon, vol. 14, no. 2, Oct. 1975, pp. 263-289.

- Cooper, M. R.; Kovach, R. L.; and Watkins, J. S.: Lunar Near-Surface Structure. Rev. Geophys. Space Phys., vol. 12, Aug. 1974, pp. 291-308.
- Cremers, C. J.; and Birkebak, R. C.: Thermal Conductivity of Fines from Apollo 12. Proceedings of the Second Lunar Science Conference, vol. 3, A. A. Levinson, ed., MIT Press (Cambridge, Mass.), 1971, pp. 2311-2315.
- Cremers, C. J.; and Hsia, H. S.: Thermal Conductivity and Diffusivity of Apollo 15 Fines at Low Density. Proceedings of the Fourth Lunar Science Conference, vol. 3, Pergamon Press (New York), 1973, pp. 2459-2464.
- Gast, P. W.: Limitations on the Composition of the Upper Mantle. J. Geophys. Res., vol. 65, no. 4, Apr. 1960, pp. 1287-1297.
- Gold, T.; Bilson, E.; and Baron, R. L.: Electrical Properties of Apollo 17 Rock and Soil Samples and a Summary of the Electrical Properties of Lunar Material at 450 MHz Frequency. Lunar Science-VII (Rev. abs. of papers presented at the Seventh Lunar Science Conference (Houston, Tex.), Mar. 15-19, 1976), pp. 298-300.
- Gold, T.; O'Leary, B. T.; and Campbell, M.: Some Physical Properties of Apollo 12 Lunar Samples. Proceedings of the Second Lunar Science Conference, A. A. Levinson, ed., vol. 3, MIT Press (Cambridge, Mass.), 1971, pp. 2173-2184.
- Haji-Scheikh, Abdolhossein: Application of Monte Carlo Methods to Thermal Conduction Problems. Ph. D. Dissertation, Univ. of Minnesota, 1965.
- Hanks, T. C.; and Anderson, D. L.: Origin, Evolution, and Present Thermal State of the Moon. Phys. Earth Planet. Interiors, vol. 5, no. 5, Oct. 1972, pp. 409-425.
- Hays, J. F.: Radioactive Heat Sources in the Lunar Interior. Phys. Earth Planet. Interiors, vol. 5, no. 1, Jan. 1972, pp. 77-84.
- Horai, K.; Simmons, G.; Kanamori, H.; and Wones, D.: Thermal Diffusivity and Conductivity of Lunar Material. Science, vol. 167, no. 3918, Jan. 30, 1970, pp. 730-731.
- Horai, K.; and Winkler, J. L., Jr.: Thermal Diffusivity of Four Apollo 17 Rock Samples. Proceedings of the Seventh Lunar Science Conference, 1976, (to be published).

- Jaeger, J. C.: Conduction of Heat in an Infinite Region Bounded Internally by a Circular Cylinder of a Perfect Conductor. Australian J. Phys., vol 9, no. 2, June 1956, pp. 167-179.
- Jeffreys, H.: The Disturbance of the Temperature Gradient in the Earth's Crust by Inequalities of Height. Monthly Notices, Roy. Astron. Soc., Geophys. Supp., vol. 4, no. 4, 1937.
- Katsube, T. J.; and Collett, L. S.: Electrical Properties of Apollo 11 and Apollo 12 Lunar Samples. Proceedings of the Second Lunar Science Conference, A. A. Levinson, ed., vol. 3, MIT Press (Cambridge, Mass.), 1971, pp. 2367-2379.
- Kaula, W. M.; Schubert, G.; Lingenfelter, R. E.; Sjogren, W. L.; and Wollenhaupt, W. R.: Apollo Laser Altimetry and Inferences as to Lunar Structure. Proceedings of the Fifth Lunar Science Conference, vol. 3, Pergamon Press (New York), 1974, pp. 3049-3058.
- Keihm, S. J.; Chute, J. L.; Peters, K.; and Langseth, M. G., Jr.: Apollo 15 Measurement of Lunar Surface Brightness Temperatures: Thermal Conductivity of the Upper 1-1/2 Meters of Regolith. Earth Planet. Sci. Letters, vol. 19, no. 3, July 1973, pp. 337-351.
- Keihm, S. J.; and Langseth, M. G., Jr.: Surface Brightness Temperatures at the Apollo 17 Heat Flow Site: Thermal Conductivity of the Upper 15 cm of Regolith. Proceedings of the Fourth Lunar Science Conference, Pergamon Press (New York), vol. 3, 1973, pp. 2503-2513.
- Keihm, Stephen J.; and Langseth, Marcus G.: Lunar Microwave Brightness Temperature Observations Reevaluated in the Light of Apollo Program Findings. Icarus, vol. 24, no. 2, 1975, pp. 211-230.
- Klaven, L.; Lofgren, L.; and Felsenthal, P.: A Rugged, Stable, Differential Platinum Resistance Thermometer. Rev. Sci. Instr., vol. 41, no. 4, 1970, pp. 541-544.
- Krotikov, V. D.; and Troitskii, V. S.: Detecting Heat Flow from the Interior of the Moon. Soviet Astron., vol. 7, no. 6, May/June 1964, pp. 822-826.
- Lachenbruch, A. H.: Rapid Estimation of the Topographic Disturbance to Superficial Thermal Gradients. Rev. Geophys., vol. 6, no. 3, Aug. 1968, pp. 365-400.
- Lachenbruch, Arthur Herold: Three-Dimensional Heat Conduction in Permafrost Beneath Heated Buildings. U.S. Geol. Survey Bull. 1052-B, 1957, pp. 51-69.

- Lachenbruch, Arthur H.: The Effect of Two Dimensional Topography on Superficial Thermal Gradients. U.S. Geol. Survey Bull. 1203-E, 1969, pp. E1-E86.
- Langseth, M. G., Jr.; More, K. A.; and Johnson, W. E.: An Experiment to Measure Heat Flow from the Interior of the Moon. Bendix Technical Journal, vol. 1, no. 1, 1968, pp. 33-43.
- Langseth, M. G., Jr.; Wechsler, A. E.; Drake, E. M.; Simmons, G.; et al.: Apollo 13 Lunar Heat Flow Experiment. Science, vol. 168, no. 3928, Apr. 10, 1970, pp. 211-217.
- Langseth, M. G., Jr.; and Von Herzen, R. P.: Heat Flow Through the Floor of the World Oceans. The Sea, vol. 4, part I, 1971, pp. 299-352.
- Langseth, M. G., Jr.; Clark, S. P., Jr.; Chute, J. L., Jr.; Keihm, S. J.; and Wechsler, A. E.: Heat-Flow Experiment. Sec. 11 of Apollo 15 Preliminary Science Report. NASA SP-289, 1972.
- Langseth, M. G., Jr.; Drake, E. M.; Nathanson, D.; and Fountain, J. A.: Development of an In Situ Thermal Conductivity Measurement for the Lunar Heat Flow Experiment. Thermal Characteristics of the Moon. AIAA Progress in Astronautics and Aeronautics Series, vol. 28, MIT Press (Cambridge, Mass.), 1972, pp. 169-204.
- Langseth, Marcus G., Jr.; Keihm, Stephen J.; and Chute, John L., Jr.: Heat Flow Experiment. Sec. 9 of Apollo 17 Preliminary Science Report, NASA SP-330, 1973.
- Latham, G. V.; Ewing, M.; Press, R.; Sutton, G.; et al.: Passive Seismic Experiment. Sec. 9 of the Apollo 16 Preliminary Science Report. NASA SP-315, 1972.
- Lee, W. H. K.; and Uyeda, S.: Review of Heat Flow Data. Terrestrial Heat Flow, American Geophysical Union (Washington, D.C.), 1965, pp. 68-190.
- Linsky, J. L.: Models of the Lunar Surface Including Temperature-Dependent Thermal Properties. Icarus, vol. 5, no. 6, Nov. 1966, pp. 606-634.
- Linsky, Jeffrey L.: The Moon as a Proposed Radiometric Standard for Microwave and Infrared Observations of Extended Sources. Astrophys. J., Supp. No. 216, vol. 25, 1973, pp. 163-203.

- Metzger, A. E.; Trombka, J. I.; Peterson, L. E.; Reedy, R. C.; and Arnold, J. R.: Lunar Surface Radioactivity: Preliminary Results of the Apollo 15 and Apollo 16 Gamma-Ray Spectrometer Experiments. *Science*, vol. 179, no. 4075, Feb. 23, 1973, pp. 800-803.
- Metzger, A. E.; Trombka, J. I.; Reedy, R. C.; and Arnold, J. R.: Element Concentrations from Lunar Orbital Gamma-Ray Measurements. *Proceedings of the Fifth Lunar Science Conference*, vol. 2, Pergamon Press (New York), 1974, pp. 1067-1078.
- Mizutani, Hitoshi; and Osako, Masahiro: Elastic-Wave Velocities and Thermal Diffusivities of Apollo 17 Rocks and Their Geophysical Implications. *Proceedings of the Fifth Lunar Science Conference*, vol. 3, Pergamon Press (New York), 1974, pp. 2891-2901.
- Robie, R. A.; Hemingway, B. S.; and Wilson, W. H.: Specific Heats of Lunar Surface Materials from 90 to 350 Degrees Kelvin. *Science*, vol. 167, no. 3918, Jan. 30, 1970, pp. 749-750.
- Smith, B. D.: The Lunar Heat Flow Experiment. *Bendix Tech. J.*, vol. 4, no. 2, 1971, pp. 64-79.
- Solomon, Sean C.: Mare Volcanism and Lunar Crustal Structure. *Proceedings of the Sixth Lunar Science Conference*, vol. 1, Pergamon Press (New York), 1975, pp. 1021-1042.
- Strangway, D. W.; Chapman, W. B.; Olhoeft, G. R.; and Carnes, J.: Electrical Properties of Lunar Soil Dependence on Frequency, Temperature, and Moisture. *Earth Planet. Sci. Letters*, vol. 16, no. 2, Oct. 1972, pp. 275-281.
- Talwani, Manik; Thompson, George; Dent, Brian; Kahle, Hans-Gert; and Buck, Sheldon: Traverse Gravimeter Experiment. Sec. 13 of Apollo 17 Preliminary Science Report. NASA SP-330, 1973.
- Taylor, S. R.: Geochemical Constraints on the Composition of the Moon. *Lunar Science-VII* (Rev. abs. of papers presented at the Seventh Lunar Science Conference (Houston, Tex.), Mar. 15-19, 1976), pp. 855-857.
- Taylor, S. R.; and Jakes, P.: The Geochemical Evolution of the Moon. *Proceedings of the Fifth Lunar Science Conference*, vol. 2, Pergamon Press (New York), 1974, pp. 1287-1305.
- Tikhonova, T. V.; and Troitskii, V. S.: Effect of Heat from Within the Moon on Its Radio Emission for the Case of Lunar Properties Which Vary with Depth. *Soviet Astron.*, vol. 13, no. 1, July/Aug. 1969, pp. 120-128.

Turcotte, D. L.; Hsui, A. T.; Torrance, K. E.; and Oxburgh, E. R.: Thermal Structure of the Moon. J. Geophys. Res., vol. 77, no. 35, Dec. 10, 1972, pp. 6931-6939.

Urey, H. C.: Proc. Natl. Acad. Sci. U.S., vol. 42, 1956, p. 889.

Wasserburg, G. J.; MacDonald, G. J. F.; Hoyle, F.; and Fowler, W. A.: Relative Contributions of Uranium, Thorium, and Potassium to Heat Production in the Earth. Science, vol. 143, no. 3605, Jan. 31, 1964, pp. 465-467.

Watson, K. I.: Thermal Conductivity Measurements of Selected Silicate Powders in Vacuum from 150-350 K, II. An Interpretation of the Moon's Eclipse and Lunation Cooling Curve as Observed Through the Earth's Atmosphere from 8-14 Microns. Ph. D. Dissertation, California Institute of Technology, 1964.

Weaver, H.: The Interpretation of Thermal Emissivity from the Moon. Solar System Radio Astronomy, Plenum Press (New York), 1965, pp. 295-354.

Williams, David L.; and Von Herzen, Richard P.: Heat Loss from the Earth; New Estimate. Geology, vol. 2, no. 7, 1974, pp. 327-328.

TABLE 10-I.- PREDICTED EXPERIMENT RANGES

Temperature gradient $\frac{dT}{dz}$, K/m	Heat flow J, $\frac{W}{m^2}$	Thermal conductivity k, $\frac{W}{m-K}$
0.1	4.2×10^{-3}	42×10^{-3}
12	25	2.1

TABLE 10-II.- PERFORMANCE REQUIREMENTS OF THE HEAT FLOW INSTRUMENT

Measurement	Requirement			
	Range	Resolution	Accuracy ¹	Minimum stability
Temperature difference across 0.5-m probe section in lowest meter of hole	±2 K (high sensitivity) ±20 K (low sensitivity)	0.0005 K (high sensitivity) 0.005 K (low sensitivity)	±0.003 K	0.003 K/yr
Ambient temperature of probe in lowest meter of hole	200 to 250 K	0.02 to 0.08 K	±0.1 K	0.05 K/yr
Temperature of thermocouples in upper 2 m of hole	90 to 350 K	±0.17 K	±0.5 K	0.5 K/yr
Thermal conductivity of material surrounding probes	0.002 to 0.4 W/m-K	±20 percent	±20 percent	--

¹Maximum probable error.

TABLE 10-III.- APOLLO 16 HEAT FLOW INSTRUMENT TEST RESULTS IN LUNAR-NIGHT ENVIRONMENT

[Test performed on July 26, 1971]

(a) Sensor data

Data	Upper gradient bridge, K	Lower gradient bridge, K	Upper remote bridge, K	Lower remote bridge, K
Absolute temperature, mean difference ¹	-0.002	-0.020	-0.028	-0.036
Absolute temperature, standard deviation ²	.016	.037	.034	.032
High-sensitivity temperature differential, mean difference ¹	.001	-.001	.003	.002
High-sensitivity temperature differential, standard deviation ²	.0002	.0002	.0021	.0010
Low-sensitivity temperature differential, mean difference ¹	.001	-.003	--	--
Low-sensitivity temperature differential, standard deviation ²	.002	.002	--	--
Cycles	8	8	10	10

(b) Thermocouple data (9 cycles)

Data	Thermocouple 1, K	Thermocouple 2, K	Thermocouple 3, K	Thermocouple 4, K
Thermocouple temperature, mean difference ¹	-0.073	1.946	-2.928	0.343
Thermocouple temperature, standard deviation ²	.190	.193	.220	.193

¹Mean difference in readings of two opposed sensors.

²Standard deviation of difference in readings of two opposed sensors about the mean difference.

TABLE 10-IV.- APOLLO 15 HFE SUBSURFACE TEMPERATURE DATA

(a) Temperature difference measurements

Bridge	Interval, cm	Equilibrium temperature difference, K	Corrected temperature difference, K ¹	Annual wave correction, K
Probe 1				
DTG12	91 to 138	0.803	0.833	-0.37
DTR12	100 to 129	.484	.479	-.28

¹The effect of the annual wave on Sept. 29, 1971, has been removed.

(b) Absolute temperature measurements

Sensor type	Depth, cm	Equilibrium temperature, K	Corrected temperature, K
Probe 1			
Platinum resistance	91	252.20	252.16
Platinum resistance	100	252.33	252.33
Platinum resistance	129	252.81	252.81
Platinum resistance	138	253.00	253.01

TABLE 10-V.- APOLLO 17 HFE SUBSURFACE TEMPERATURE DATA

(a) Temperature difference measurements

Bridge	Interval, cm	Equilibrium temperature difference ¹ , K	Corrected temperature difference ² , K	Annual wave correction, K
Probe 1				
DTG11	130 to 177	0.707	0.755	-0.027
DTR11	139 to 168	.435	.467	-.018
DTG12	185 to 233	.533	.559	-.001
DTR12	194 to 224	.322	.326	<.001
Probe 2				
DTG21	131 to 178	0.370	0.390	-0.027
DTR21	140 to 169	.218	.223	-.018
DTG22	186 to 234	.336	.359	-.001
DTR22	195 to 225	.206	.212	<.001

¹The error associated with extrapolating to equilibrium temperature differences is ± 0.003 K.

²The uncertainty introduced by these corrections is estimated to be ± 2 percent.

(b) Absolute temperature measurements

Sensor type	Depth, cm	Equilibrium temperature ¹ , K	Corrected temperature ² , K
Probe 1			
Thermocouple TC4	66	254.20	254.20
Platinum resistance	130	255.06	255.02
Platinum resistance	139	255.19	255.17
Platinum resistance	168	255.62	255.64
Platinum resistance	177	255.76	255.78
Platinum resistance	185	255.91	255.91
Platinum resistance	194	256.03	256.04
Platinum resistance	224	256.36	256.37
Platinum resistance	233	256.44	256.47
Probe 2			
Thermocouple TC4	57	254.70	254.70
Platinum resistance	131	256.07	256.05
Platinum resistance	140	256.09	256.09
Platinum resistance	169	256.31	256.31
Platinum resistance	179	256.44	256.44
Platinum resistance	186	256.48	256.48
Platinum resistance	195	256.52	256.51
Platinum resistance	225	256.73	256.73
Platinum resistance	234	256.82	256.84

¹The accuracy of extrapolated absolute temperatures is ± 0.05 K for the platinum resistances.

²The correction for the annual wave to be applied to the thermocouple is 0.04 K.

TABLE 10-VI.- CONDUCTIVITIES FROM COOLDCWN HISTORIES

Sensor depth, cm	Heater location	Conductivity with drill heating effects, W X 10 ⁻⁴ /cm-K	Conductivity without drill heating effects, W X 10 ⁻⁴ /cm-K
Probe 1			
66	H11	1.0	--
130		2.3	1.3
139		1.9	1.1
168	H12 H13	1.9	1.1
177		2.0	1.0
185		1.9	1.1
194	H14	2.1	1.1
224		2.8	1.4
233		2.7	1.6
Probe 2			
67	H21	1.0	--
131		2.0	1.2
140		2.0	1.1
169	H22 H23	2.4	1.3
178		2.7	1.7
186		2.9	1.7
195	H24	2.7	1.5
225		2.8	1.5
234		2.5	1.5

TABLE 10-VII.- RESULTS OF THE CONDUCTIVITY EXPERIMENTS

Heater location	Depth, cm	Conductivity, ¹ W X 10 ⁻⁴ /cm-K	Contact conductance, ² W X 10 ⁻⁴ /cm ² -K
Apollo 17 probe 1			
H11	130	2.50	1.4
H12	177	1.72	1.6
H13	185	1.79	1.4
H14	233	2.95	1.2
Apollo 17 probe 2			
H21	131	2.06	1.6
H22	178	2.36	1.1
H23	186	2.64	1.5
H24	234	2.24	2.3
Apollo 15 probe 1			
H11	35	1.41	0.8
H12	83	2.11	.8
H13	91	1.60	.9
H14	138	2.50	1.0
Apollo 15 probe 2			
H23	49	1.46	0.5
H24 ³	96	2.43	.6

¹The estimated error of conductivity measurement is ± 15 percent.

²Estimated error is ± 20 percent. In the theoretical model, the thickness of the contact zone is 2 mm.

³It is probable that a section of broken borestem lies just outside this location so that the uncertainty of this measurement is very large.

TABLE 10-VIII.- HEAT FLOW DATA

Depth interval, cm	Temperature gradient, K/cm	Average conductivity, $W \times 10^{-6}/cm-K$	Heat flow, $W \times 10^{-6}/cm^2$
Apollo 17 probe 1			
66 to 130	0.0130	1.60	2.10
130 to 177	.0158	1.79	2.83
139 to 168	.0163	1.72	2.80
185 to 233	.0118	2.39	2.81
194 to 224	.0113	2.48	2.81
66 to 233	.0140	1.80	2.50
Apollo 17 probe 2			
67 to 131	0.0210	1.50	3.10
131 to 178	.0082	2.26	1.86
140 to 169	.0078	2.30	1.79
186 to 234	.0076	2.50	1.89
195 to 225	.0074	2.53	1.87
67 to 234	.0130	2.00	2.50
Apollo 15 probe 1			
91 to 138	0.0175	1.78	3.11
100 to 129	.0166	1.68	2.82

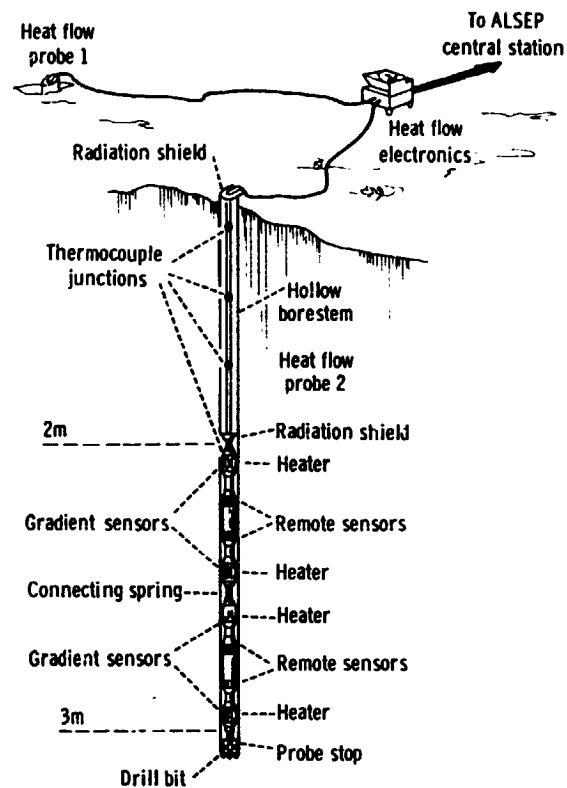


Figure 10-1.- Optimum site configuration for lunar HFE.

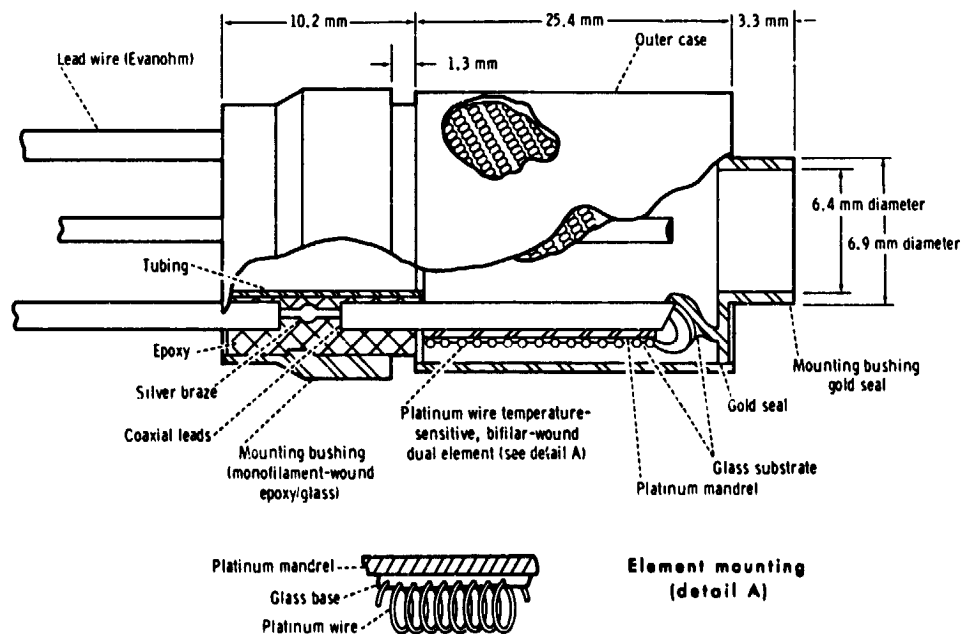


Figure 10-2.- Gradient-sensor construction.

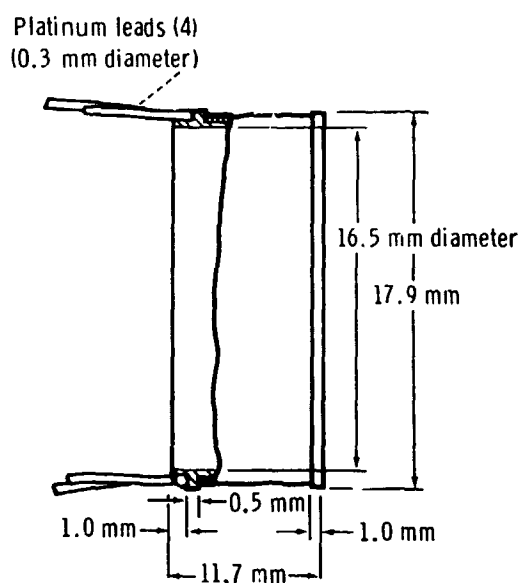


Figure 10-3.- Ring- or remote-sensor construction.

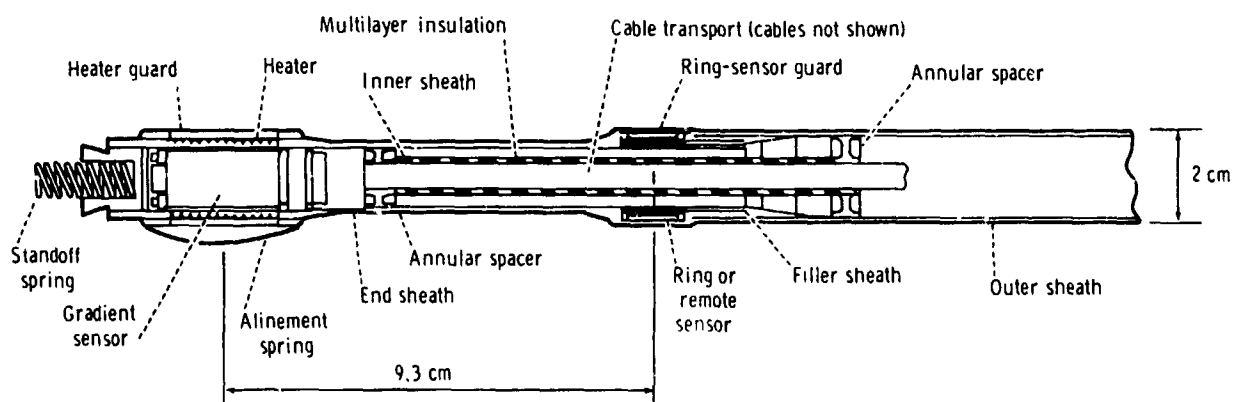


Figure 10-4.- Half-probe end section.

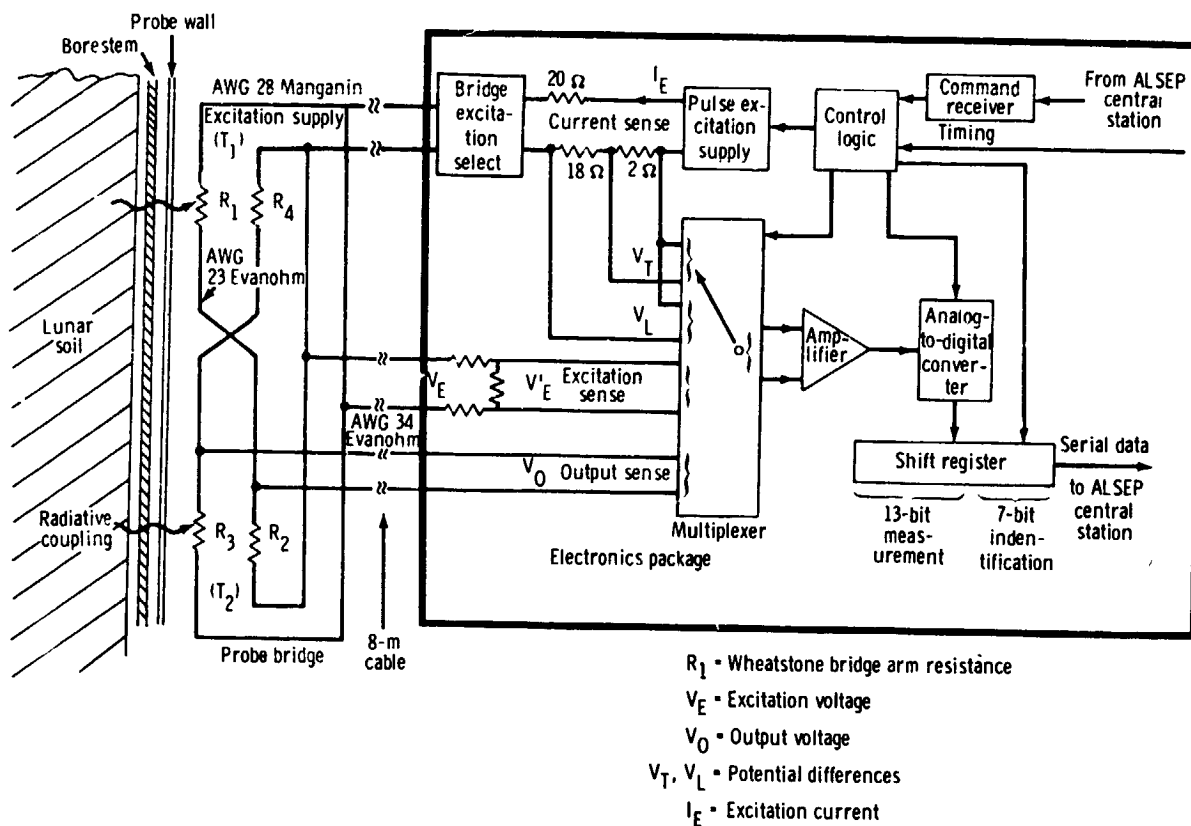


Figure 10-5.- Schematic of electronics measurements on bridge sensors.

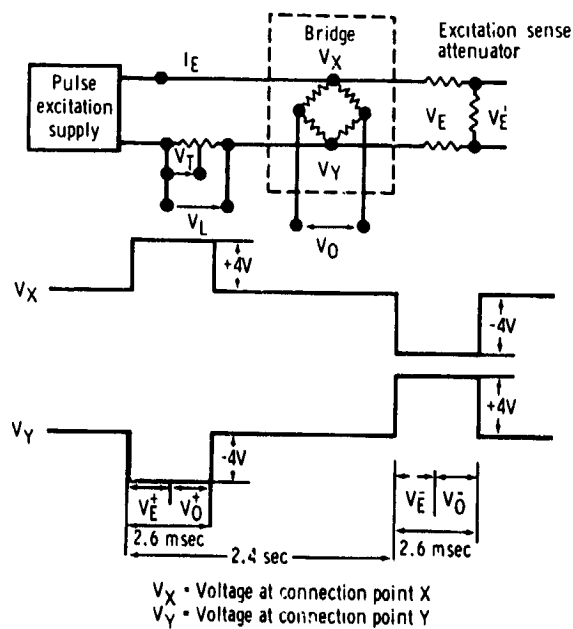
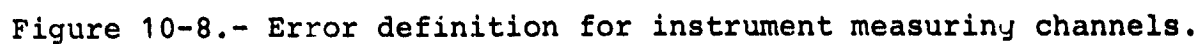
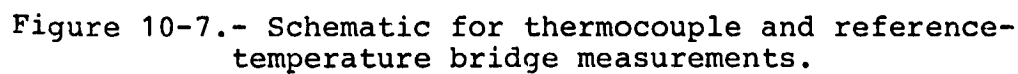
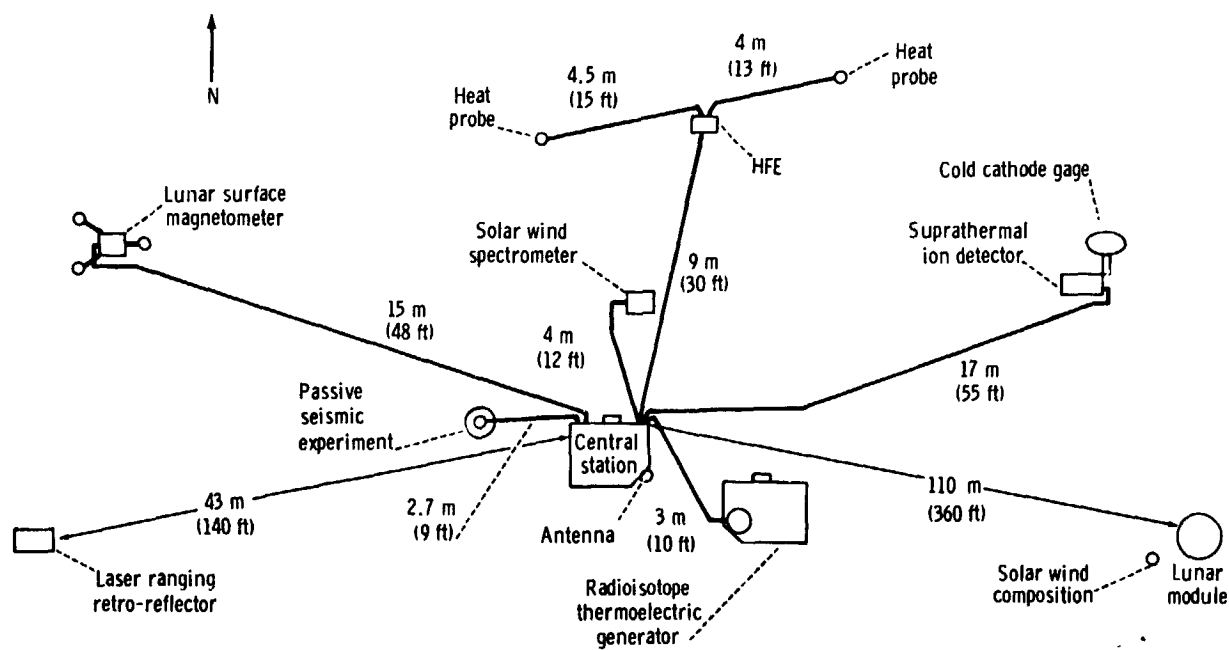


Figure 10-6.- Typical sequence for bridge measurements.





Note: The solar wind composition experiment was located about 15 m (50 ft) from the lunar module

Figure 10-9.- Apollo 15 ALSEP deployment.

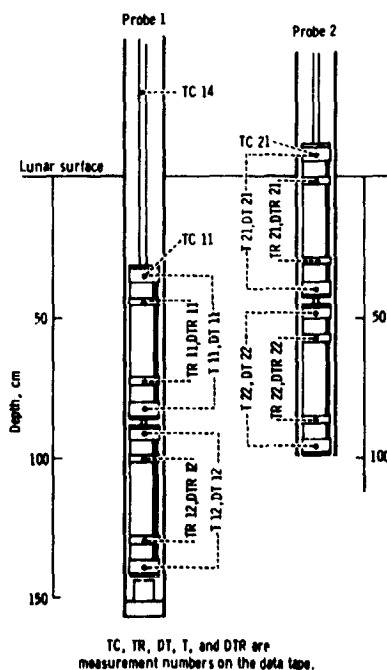


Figure 10-10.- Subsurface configuration of the HFE probes for Apollo 15.

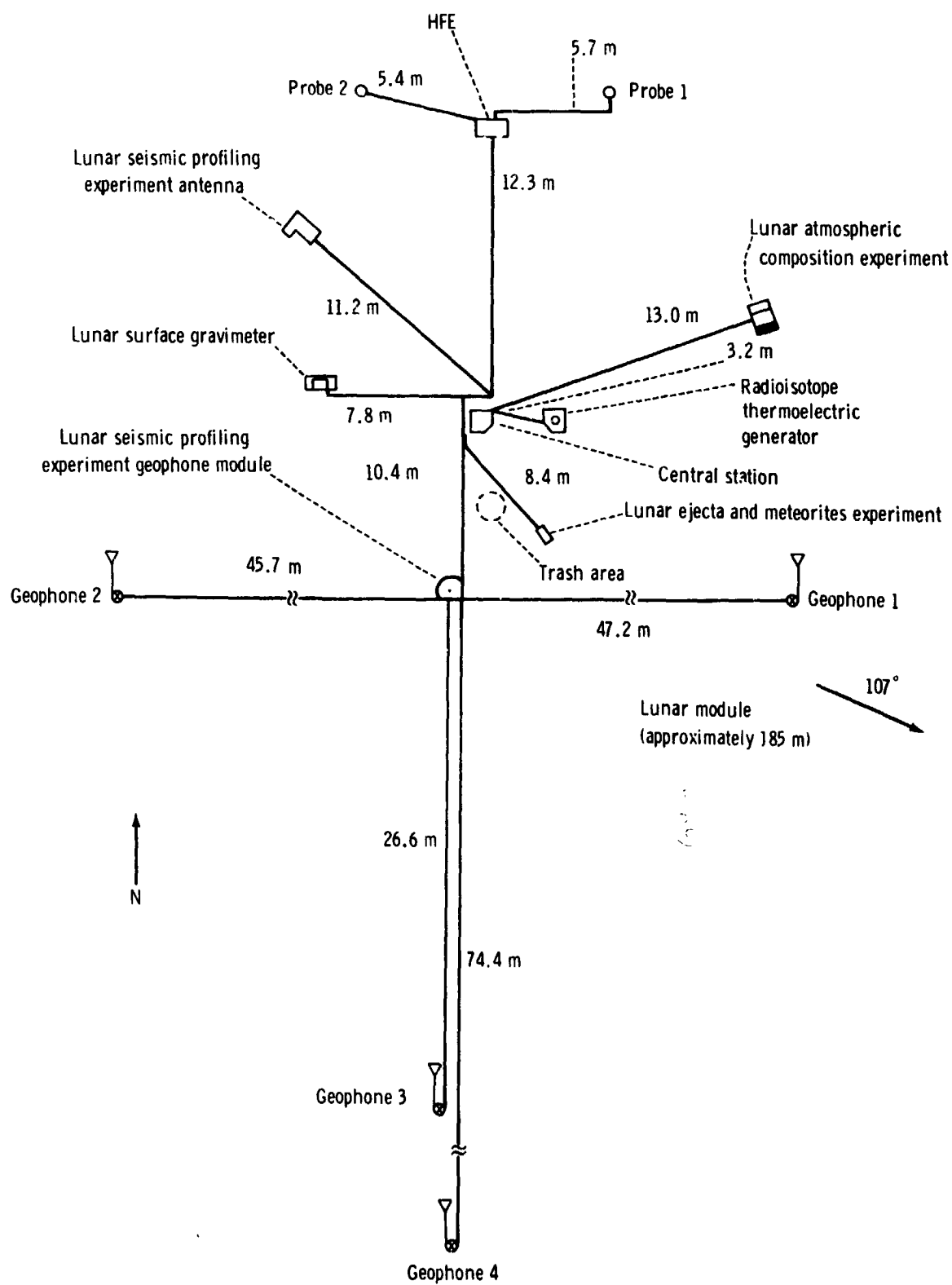


Figure 10-11.- Apollo 17 ALSEP experiment geometry.

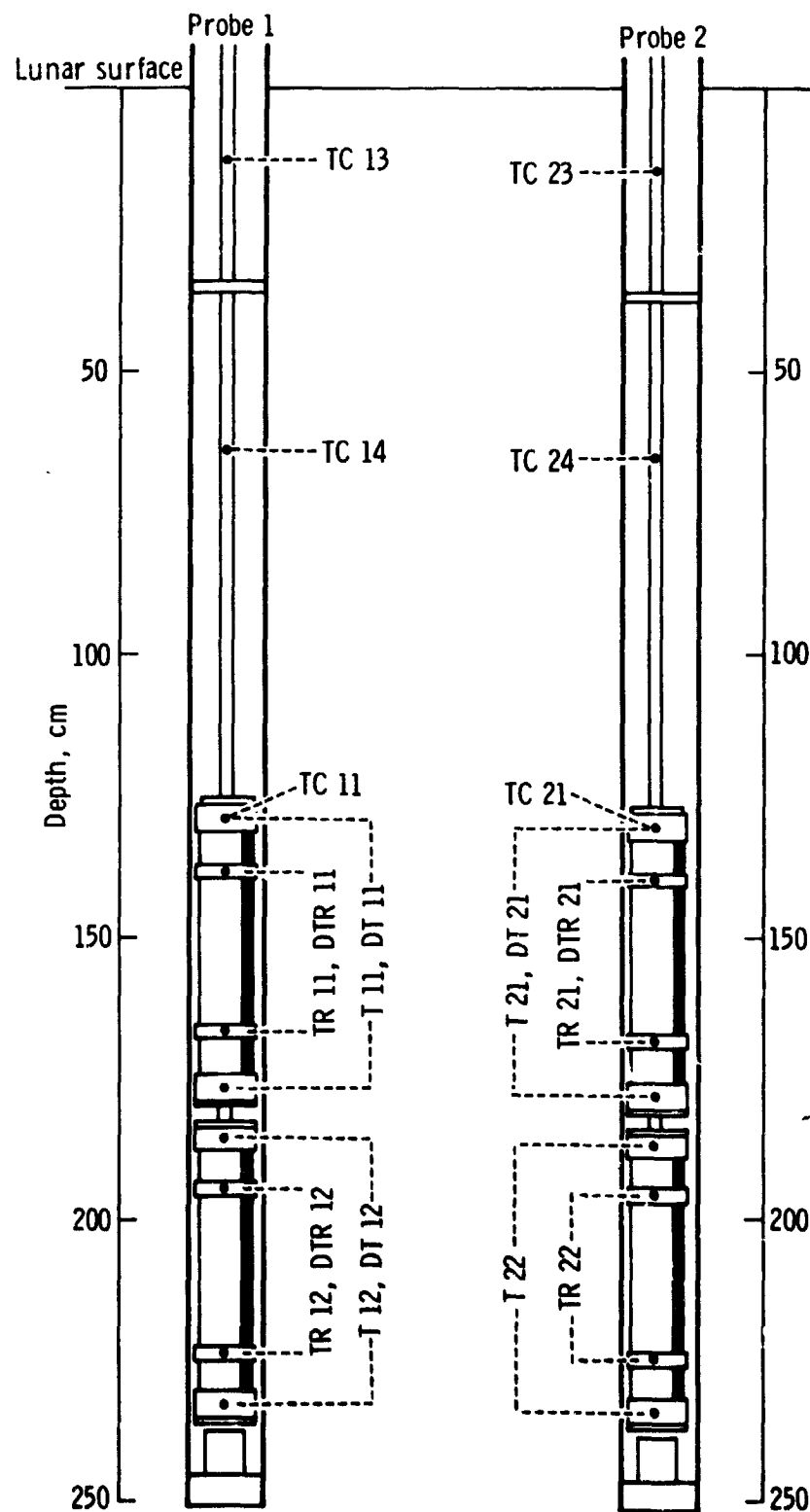


Figure 10-12.- Subsurface geometry of the HFE probes for Apollo 17.

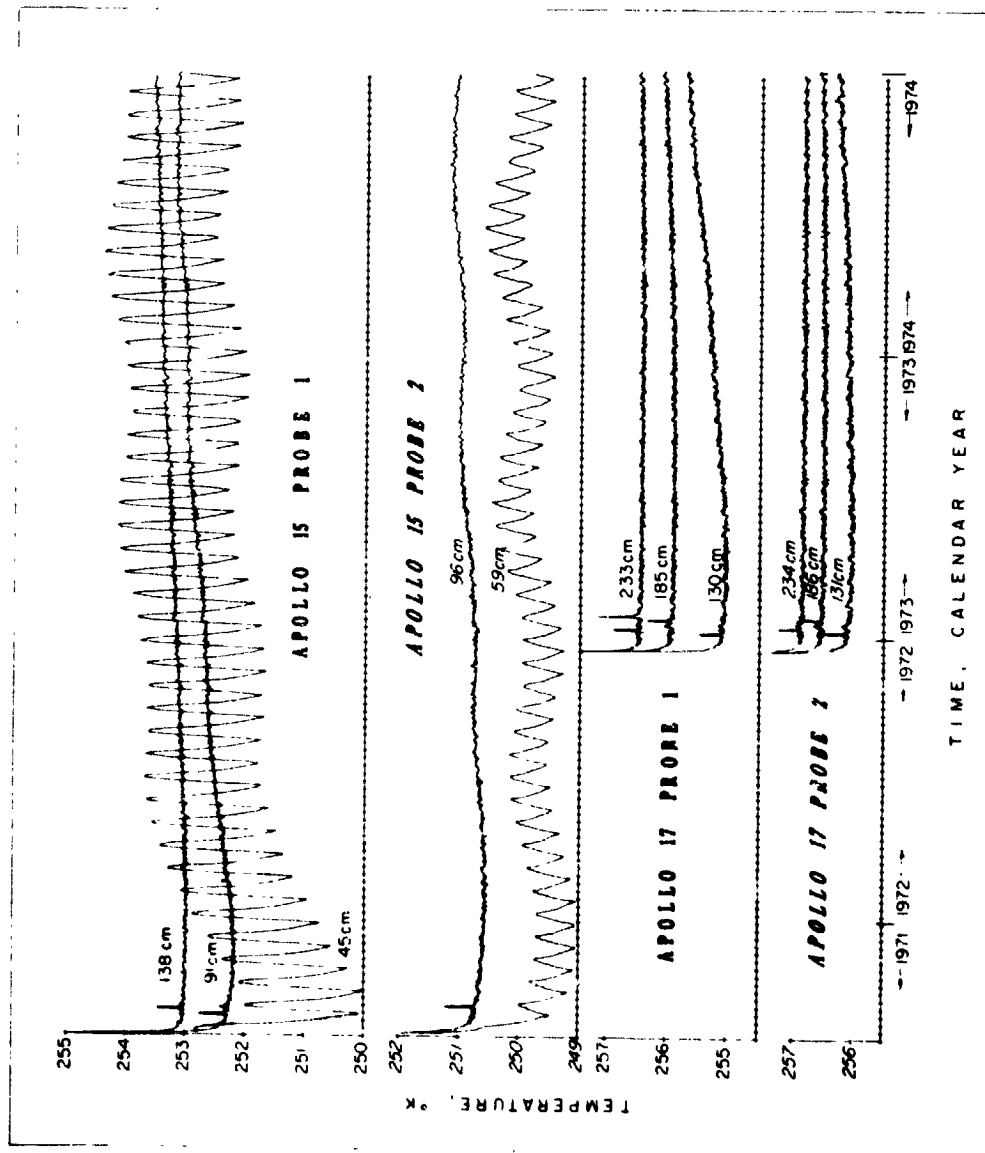


Figure 10-13.- Subsurface temperature histories covering a 3.5-yr period of representative sensors on the four heat flow probes. Initial cooldown of the probes after insertion is indicated at the start of each history. The small spikes in the first 60 days result from the short-term conductivity experiments.

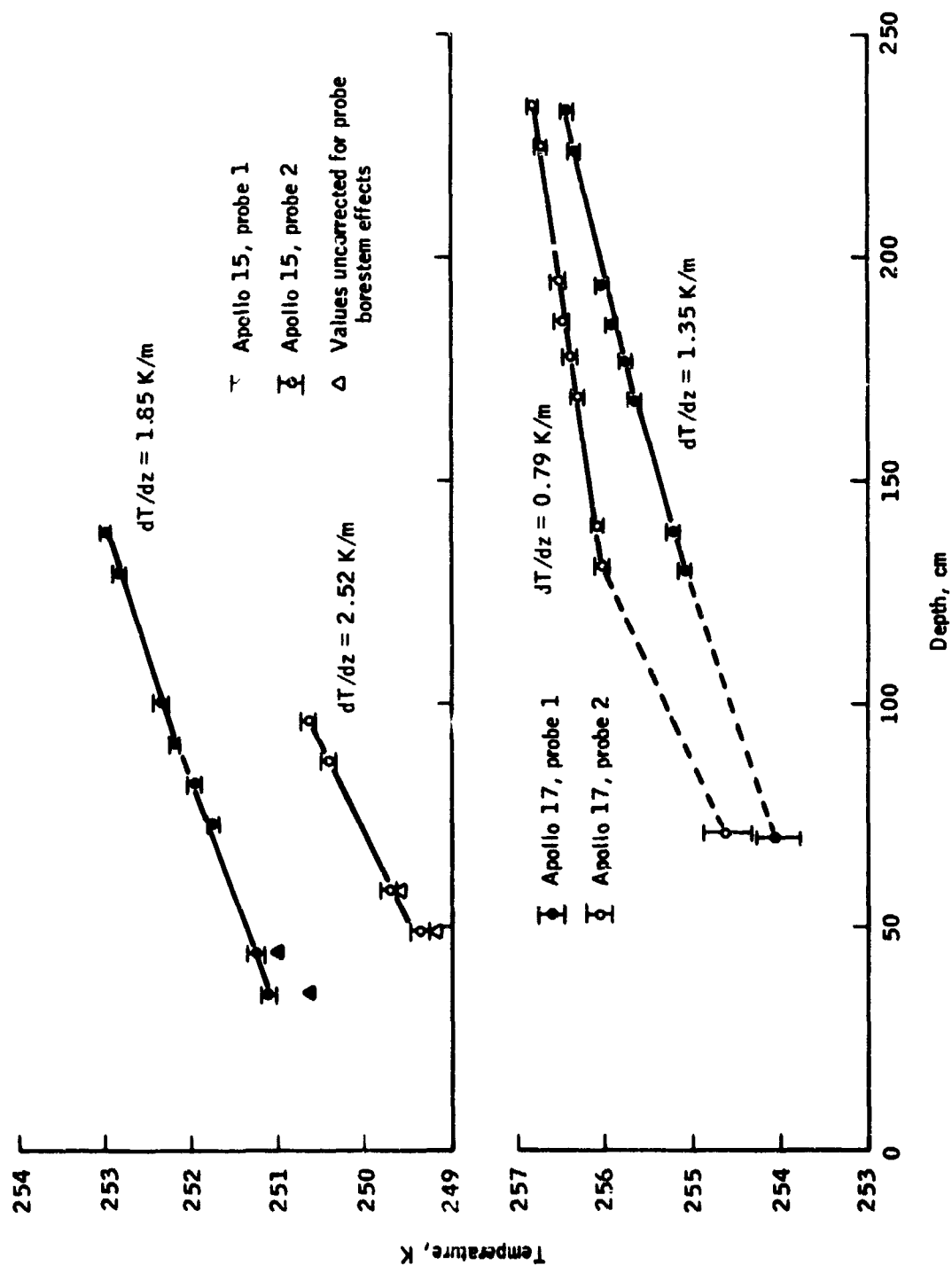


Figure 10-14.- Mean subsurface temperatures at the four probes as a function of depth. Note that temperatures of sensors shallower than 65 cm have been corrected upward to account for a steady radiative heat loss to the surface.

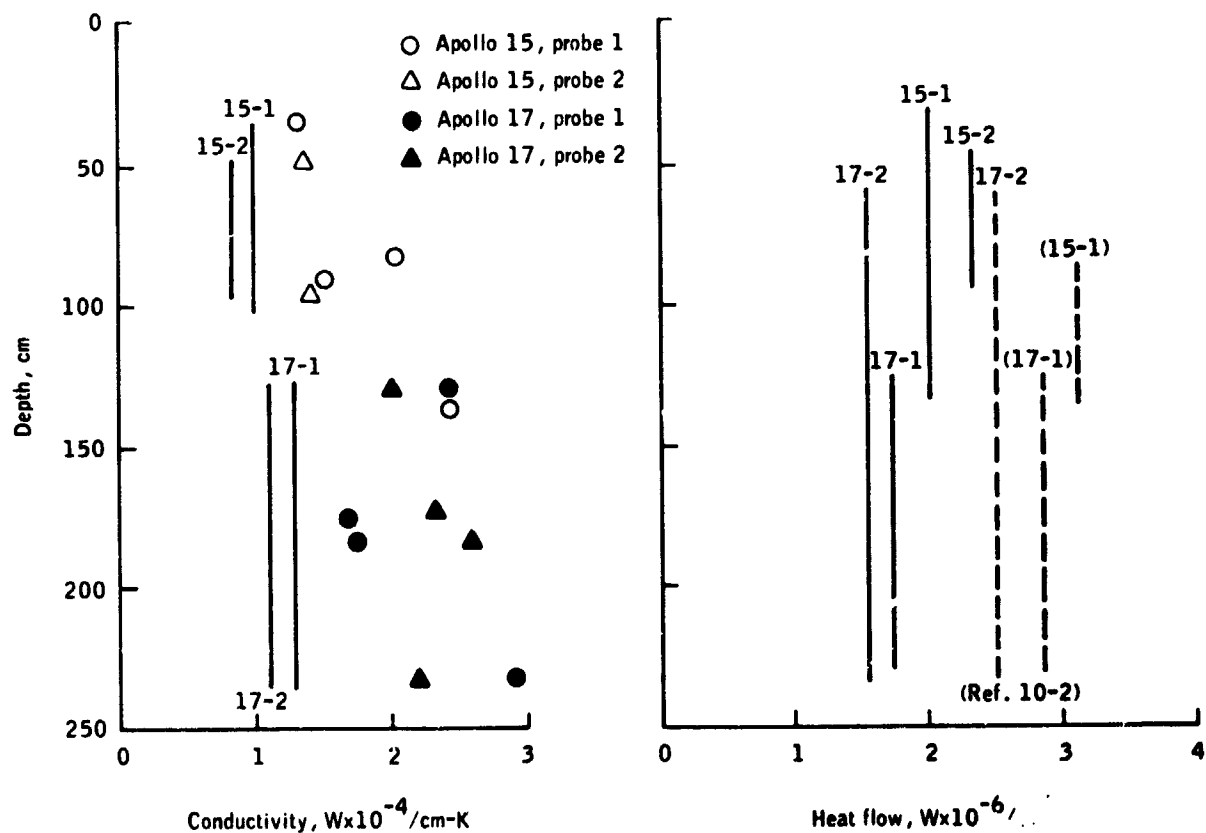
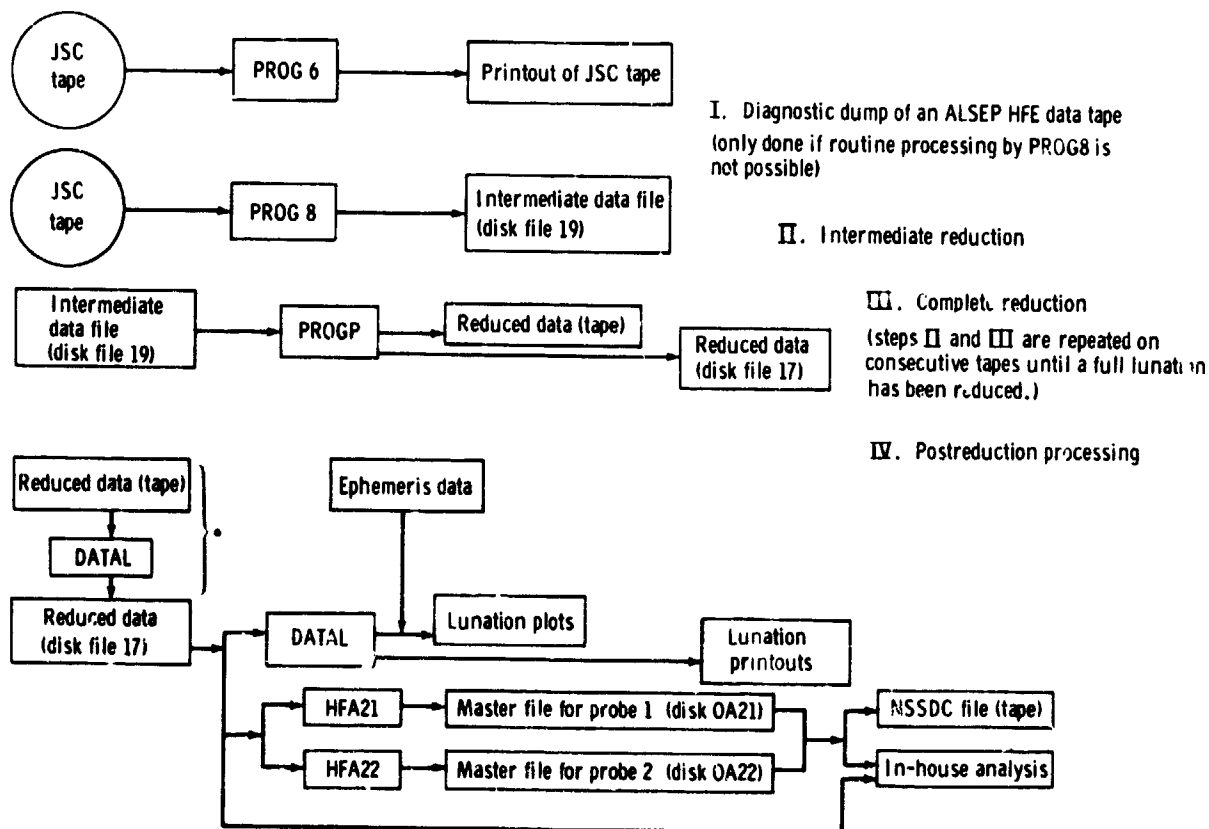


Figure 10-15.- Revised conductivity values are shown on the left as solid lines over the intervals where applicable. The short-term point measurements (ref. 10-2) are shown for comparison. The revised heat flow values (solid lines) are shown on the right together with the preliminary results (dashed lines) that were based on interpolation of the short-term conductivity measurements. (Mission and probe numbers are designated 15-1, 15-2, etc.)



* Not part of routine processing; only done if necessary.

Figure 10-16.- Flow diagram for reduction of one lunation of data.